Nanoscale

REVIEW

View Article Online
View Journal

Cite this: DOI: 10.1039/d5nr03181h

Nanostructured systems to combat NO_x air pollution through Vis-light activated nanoarchitectonics: how, where and why...?

Davide Barreca, [a] Beatriz Gámiz, [b] Chiara Maccato *[a,c] and Luis Sánchez [b]

Nitrogen oxide (NO_x) gases generated from various anthropogenic sources have a highly detrimental impact on both human health and the environment. Among the possible routes for their efficient removal from the atmosphere ($DeNO_x$), a mandatory issue in compliance with the ever more stringent regulations, photocatalytic processes offer sustainable and eco-friendly toolkits for NO_x elimination at parts per billion (ppb) levels. To date, a great deal of work has been performed on UV-activated photocatalysts based on TiO_2, but real-world applications require the use of Vis-light activated materials to effectively harness solar energy, a renewable and largely available natural resource. In this general framework, the present review provides an original summary of recent advances in the preparation, characterization and functional validation of Vis-light activated $DeNO_x$ photocatalysts free from TiO_2, an overview which, to our knowledge, is not available in the literature. In particular, the attention is concentrated on tailored nanostructure control in the target materials, with particular focus on nano- and heterocomposites enabling improved charge carrier separation and, hence, enhanced performance. The main issues in preparation and characterization, with particular regard to the catalyst stability and selectivity towards NO_x conversion into harmless nitrates, are discussed in relation to selected material categories, with an eye on multifaceted design strategies and on the outlook for Vis-light activated TiO_2-free $DeNO_x$ photocatalysts. This overview is expected to inspire frontier advancements in the mastering of Vis-light activated photocatalysts for air purification, an issue of key importance to promote effective sustainable development.

Received 28th July 2025,
Accepted 1st September 2025

DOI: 10.1039/d5nr03181h

rsc.li/nanoscale

1. Introduction

As highlighted by the Lancet Commission, pollution is a major global hazard to planetary and human health and jeopardizes the sustainability of modern societies. In fact, urban areas often cope with elevated levels of air pollutants, exceeding World Health Organization (https://www.who.int/) (WHO) recommendations, which are the root cause for millions of premature deaths worldwide.[1,2] These phenomena represent an extremely alarming threat, taking into account that dangerous climatic effects are also involved.[2] Among the various air pollutants,[3,4] gaseous nitrogen oxides (NO_x, consisting of 95% NO and NO_2),[5] produced by road transport, energy production, industries, and even agriculture,[2,3,6] have a high pathogenic effect on human health.[2,7–9] In addition, they represent a very serious environmental burden, since they contribute to ozone depletion, photochemical smog, and the acidification of soil, water, and building materials, as well as aquatic eutrophication (Fig. 1).[10–14] Although environmental EU and US agencies limit the hourly allowed NO_x air concentration to 0.1 ppm and 0.2 ppm,[8,15] these values are hardly attained, especially in highly populated cities.[16] As a consequence, both short- and long-term strategies are highly demanded in order to decrease the related disease severity and prevent new-onset disease developments.[2,7,15,17]

Currently, multiple techniques are available for NO_x capture and abatement ($DeNO_x$ action), including catalytic reduction and adsorption onto suitable materials,[6,10,12,18–22] but many of them are unsuitable for an economically viable removal of NO at low concentrations.[23] Among the various options, heterogeneous photocatalysis through suitable semiconductors, assisted by water, oxygen and sunlight, offers a green and sustainable strategy to lower NO_x air content down to ppb levels under ambient conditions.[5,15,19,24–26] Nonetheless, several photocatalysts are afflicted by various shortcomings, including limited light absorption capacity, inappropriate band gaps, and fast recombination of photogenerated charge carriers.[5,15,27] Indeed, the development of

[a]CNR-ICMATE and INSTM, Department of Chemical Sciences, Padova University, 35131 Padova, Italy
[b]Departamento de Química Inorgánica e Ingeniería Química, Instituto de Química para la Energía y Medioambiente, Universidad de Córdoba, Campus de Rabanales, 14014 Córdoba, Spain
[c]Department of Chemical Sciences, Padova University and INSTM, 35131 Padova, Italy. E-mail: chiara.maccato@unipd.it

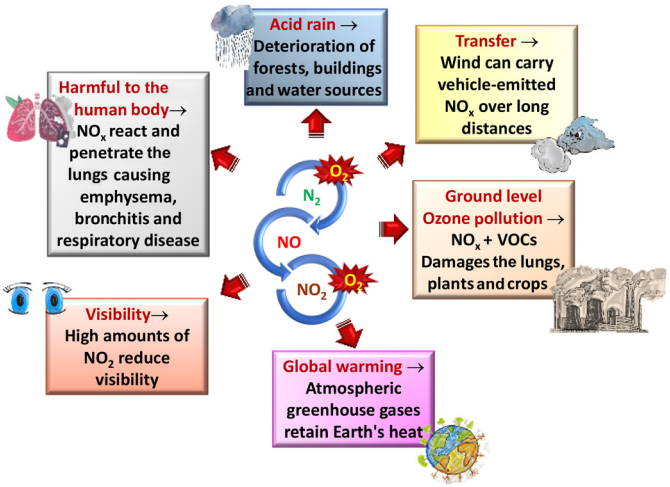

Fig. 1 Sketch of the atmospheric generation of NO_x (center) and of the related detrimental effects on the environment and human health.

economically viable and eco-friendly systems endowed with optimized $DeNO_x$ performances represents an open challenge[28] to achieving more sustainable and effective environmental remediation,[8,24] requiring appropriate modulation of the active material's features. In fact, although the total removal of NO with conversion to harmless nitrate is highly desirable,[15,24,27,29] the generation of toxic byproducts like NO_2 through non-selective oxidation by oxygen species remains a persistent issue.[11] In fact, NO_2 toxicity is approximately 25 times higher than that of NO,[30] and, consequently, regulatory standards for ambient concentrations, as established by the European Union[31] and WHO,[32] are significantly stricter for NO_2 (allowed thresholds in ambient air: ≈25 ppm and 1–3 ppm for NO and NO_2, respectively). Accordingly, catalyst efficiency and selectivity have progressed to some extent through the use of various integrated design strategies involving, among others, doping, defect engineering, and material functionalization.[3,5,24,33] However, photocatalytic NO_x abatement still mainly exists within the realm of laboratory-scale research due to various concurrent issues. In fact, the most extensively studied photocatalysts for such processes are based on titanium dioxide (TiO_2),[3] whose large band gap (E_G = 3.2 eV) requires UV light activation, accounting for only ≈4% of the whole solar spectrum.[15,22,34–38] As a consequence, $DeNO_x$ performances of TiO_2-based photocatalysts dramatically decrease under certain circumstances, particularly in cities located in North America and Central/North Europe, where only low levels of UV radiation are available.[15,39] Furthermore, TiO_2 often exhibits low selectivity towards harmless NO_3^- formation,[8,37,40] and may be carcinogenic when inhaled.[41] Thus, various research efforts are being devoted to alternative Vis-light activated $DeNO_x$ photocatalysts,[12,19,25–27,42] whose development and mastering, however, are still in their infancy in comparison with that of TiO_2-based ones.

In this general context, the present minireview aims to provide a specific perspective on the evolution made over the last decade in the design, synthesis, modification, and functional validation of nanostructured $DeNO_x$ photocatalysts based on Vis-light activated semiconductors *not* containing titanium dioxide. To the best of our knowledge, no such overviews are available in the relevant literature, whereas various reviews regarding the general aspects of the targeted processes activated by UV light and involving TiO_2-based materials have been published to date.[3,5,10,15,24,27] Far from providing a fully comprehensive literature overview and from entering into technical details of the process mechanism and surface engineering of the constructions, this work focuses on representative case studies related to various material categories (see below), providing a framework to elucidate the property–activity interplay and highlighting the actual open challenges. Specifically, after a brief resumé of the process mechanism recalling the main issues necessary for a proper understanding of the reported data, attention is dedicated to the interplay between the modulation of the composition, structure, and morphology and the resulting $DeNO_x$ photocatalytic performances in the framework of nanoarchitectonics, a key paradigm in nanomaterials science based on the combination of nanotechnologies with other specific disciplines to develop systems with tailored functional information.[16] By consolidating recent progress in this regard and highlighting future directions, the present manuscript aims to inspire new ideas and methodologies to advance research on Vis-light activated $DeNO_x$ photocatalysts, with a view towards eventual real-world applications.

2. General description of the mechanism

The photocatalytic $DeNO_x$ process involves photochemical NO_x conversion into nitrite or nitrate species, thereby removing nitrogen oxides from the surrounding atmosphere.[25] In a nutshell, the underlying mechanism can be described as follows. The first step is NO chemisorption on the surface of a suitable semiconductor (Fig. 2), whose illumination with appropriate

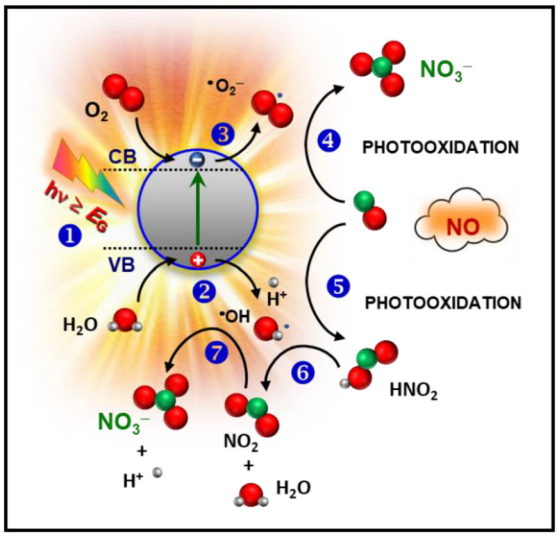

Fig. 2 Sketch of photocatalytic NO oxidation promoted by a semiconductor. CB = conduction band; VB = valence band. Reproduced with permission from ref. 16. Copyright 2023, The Royal Society of Chemistry.

photons promotes the transfer of electrons (e^-) to the CB, while creating holes (h^+) in the VB. These charge carriers, in turn, are directly involved in the reaction with water and oxygen molecules present in the surroundings to yield reactive oxygen radicals (ROSs) [mainly superoxide ($^{\bullet}O_2^-$) and hydroxyl ($^{\bullet}OH$) radicals, shown in Fig. 2]. The latter are powerful oxidizing agents capable of transforming NO_x into nitrite and nitrate species.[43] In particular, water molecules, besides participating in $^{\bullet}OH$ generation, facilitate NO adsorption *via* hydrogen bonding with hydroxyl groups. In general, hydroxyl radicals assist stepwise oxidation of NO → NO_2^- → NO_2 → NO_3^-, whereas superoxides can directly oxidize various oxide intermediates to NO_3^- (Fig. 2).[43–45] However, beyond this simplified sketch, the actual $DeNO_x$ mechanism, which has already been reported elsewhere and whose detailed description is out of the scope of the present minireview, is considerably more complex,[14,22,46] and additional intermediates such as NO^+, N_2O_3, $N_2O_2^{2-}$, N_2O_4 and NO_2^+ may be generated through multiple reaction pathways.[27,47]

The efficiency of photocatalytic NO removal is governed by a combination of physical and electronic factors, among which the interaction between reactants and active sites on the photocatalyst surface plays an important role. Materials with a high specific surface area enhance this interaction, thereby improving the system performances, whereas passivation of active sites, caused for instance by nitrite/nitrate accumulation, results in a detrimental decrease in activity over time. Yet, such species can be readily removed by dissolution in water, promoted by ambient humidity, dew or rainfall, and aid the regeneration of the photocatalyst active sites.[15]

From an electronic perspective, the band structure of the photocatalyst is critical for achieving effective $DeNO_x$ activity. Effective Vis-light absorption and minimized e^-/h^+ recombination enhance the availability of photogenerated charge carriers, triggering the redox reactions involved in NO removal. Since the latter proceeds *via* a photo-oxidation process, the redox potential of the involved species is crucial for determining the optimal CB and VB edge positions of the active materials. To achieve effective $DeNO_x$ performance, electrons should be produced in the CB at potentials more negative than that of the $E_{O_2/^{\bullet}O_2^-}$ value of the redox pair (−0.13 eV), whereas holes should be generated in the VB at potentials more positive than those of $E_{OH^-/OH}$ (1.99 eV) and $E_{H_2O/^{\bullet}OH}$ (2.82 eV) values of the redox pairs. As already mentioned, the unintentional NO_2 release during the $DeNO_x$ process is highly undesirable for its hazardous effects and hence a key objective is to maximize the system selectivity, *i.e.* the photocatalyst's capacity for fully oxidizing NO to stable, non-volatile nitrites or nitrates. In fact, achieving high selectivity is essential not only for environmental safety but also to enhance the $DeNO_x$ process efficiency and sustainability.

3. Relevant case studies on Vis-light activated, non-TiO_2 $DeNO_x$ photocatalysts

In this section, selected case studies regarding Vis-light activated $DeNO_x$ photocatalysts based on materials different from TiO_2 will be examined. As a matter of fact, the identification of a unitary vision to rationalize and discuss the pertaining papers available to date is a challenging task, due to the inhomogeneity of literature papers and to the possibility of classifying them in multiple different ways. In this minireview, data discussion is categorized based on the nature of the active photocatalyst materials, as sketched in Fig. 3. The order in which the various materials are presented herein (according to which the most investigated systems, based on the available literature reports, are discussed first) reflects the story flow in the following description. It is worthwhile highlighting that Fig. 3 has to be intended only as a general classification of the main families of Vis-light activated $DeNO_x$ photocatalysts, since the present characterization is not unique and there is a direct correlation between the reported system categories. In fact, for instance, plasmonic metal-containing photocatalysts (§ 3.2) comprise oxide-based materials (§ 3.1), some of the bismuth-based photocatalysts (see § 3.3 and note[48]) contain plasmonic metal nanoparticles, and carbon/graphene quantum dot-containing heterocomposites are often integrated with many of the materials reported in the previous sections. For each of the target material classes, attention is dedicated to a brief presentation of selected case studies, encompassing single and multi-phase materials (*i.e.*, nanocomposites and nanoheterostructures). Specifically, focus is given to the tailoring of nanomaterial's physicochemical characteristics using various fabrication procedures and the modulation of the adopted processing conditions, which offer a valuable

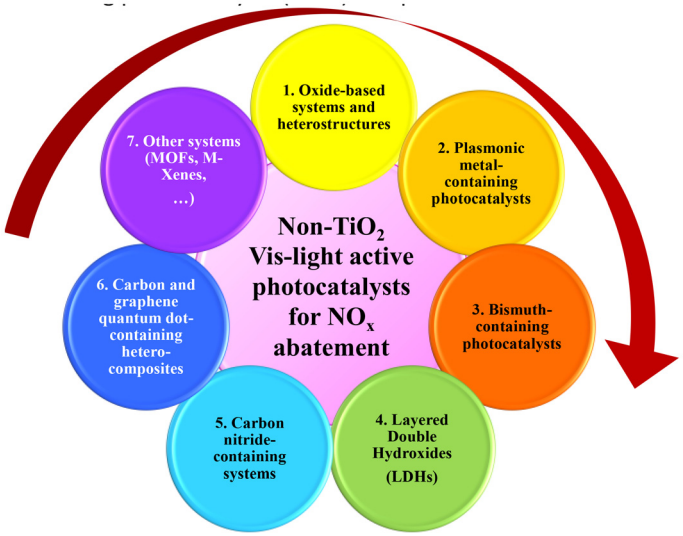

Fig. 3 Schematic overview of the materials targeted in the present work.

toolbox to modulate and boost the resulting DeNO$_x$ performances. These issues are of key importance, especially in the case of supported photocatalysts directly grown onto suitable substrates that are less hazardous, more stable, and more easily recoverable after use than widely investigated powdered counterparts.[38,49–52] Efforts have been devoted to presenting the main phenomena accounting for the system properties and activity, although the main limitations hindering a large-scale use of the present materials and technologies persist. In order to enable a more comprehensive comparison of the system performances, Table S1 reports the illumination conditions, initial NO concentrations, NO removal efficiencies, and selectivity data (when available) for photocatalysts belonging to material classes indicated in Fig. 3.

3.1 Oxide-based systems and heterostructures

Oxide-based heterostructures and perovskite materials (ABO_3-type oxides) have gained attention for their structural tunability, defects, and favorable electronic band structures, which are critical parameters for achieving effective NO$_x$ degradation under Vis illumination. This section focuses on representative examples showing how morphology, doping, and nano-heterostructure engineering influence their photocatalytic efficiency and selectivity in the NO → NO_2 → NO_3^- conversion.

A pioneering study by Fragoso *et al.*[53] introduced supported β-Fe_2O_3/CuO and β-Fe_2O_3/WO_3 nano-heterostructures, containing the metastable β polymorph instead of the most thermodynamically stable α-Fe_2O_3 one as effective photocatalysts for NO$_x$ removal under simulated solar light. These systems exhibited appreciably higher performances than bare Fe_2O_3, principally due to heterojunction-induced charge separation and elevated oxygen vacancies (OVs), whose engineering plays an important role in the ultimate material performances.[14] The type-II band alignment facilitated an efficient e^-/h^+ separation, which, in turn, promoted ROS generation, enabling selective NO → NO_3^- oxidation with no NO_2 accumulation. Tran *et al.*[54] reported the synthesis of ZnO nanorods *via* a one-step solvothermal route, yielding structures with high aspect ratios and abundant surface OVs. These features facilitated directional charge transport, whereas oxygen defects acted as sites for NO adsorption and $^{\bullet}O_2^-$ formation. Photocatalytic tests revealed that ZnO nanorods achieved 79% and 62% NO removal under solar and Vis-light irradiation, respectively, with low NO_2 generation. Electron paramagnetic resonance (EPR) experiments confirmed the participation of $^{\bullet}OH$ and $^{\bullet}O_2^-$ in the process.

In order to further improve Vis-light assisted processes, transition metal dopants have been incorporated into ZnO structures. Nguyen *et al.*[55] synthesized Cr-doped ZnO nanoparticles (NPs) *via* a sol–gel route. The substitution of Zn^{2+} by Cr^{3+} induced lattice distortions and generated mid-gap electronic states, facilitating Vis-light absorption. A complementary strategy to doping is based on the intentional OV engineering in metal oxide lattices. Song *et al.*[11] leveraged this concept through the design of Ce-doped SnO_2 photocatalysts (Fig. 4), annealed under different atmospheres to tailor the O defect content. Bare SnO_2 was composed of spherical-shaped NPs (Fig. 4a) that underwent a moderate decrease in dimensions upon doping (Fig. 4b and c). Chemical mapping (Fig. 4d) evidenced an even distribution of Sn, O, and Ce throughout the entire NPs. NO removal performances (Fig. 4e) were appreciably higher for Ce-doped SnO_2 in comparison with that of bare SnO_2, due to the modest Vis-light response of the latter, especially for systems subjected to Ar annealing. In parallel, a lower release of toxic NO_2 was also observed (Fig. 4f). These results were related to the higher content of OVs, serving both as electron traps and catalytic sites, for Ar-treated specimens, that also yielded a more efficient oxidative conversion to NO_3^- (Fig. 4g and h). Nevertheless, an issue to be properly tackled is the system stability, since the activity decreased

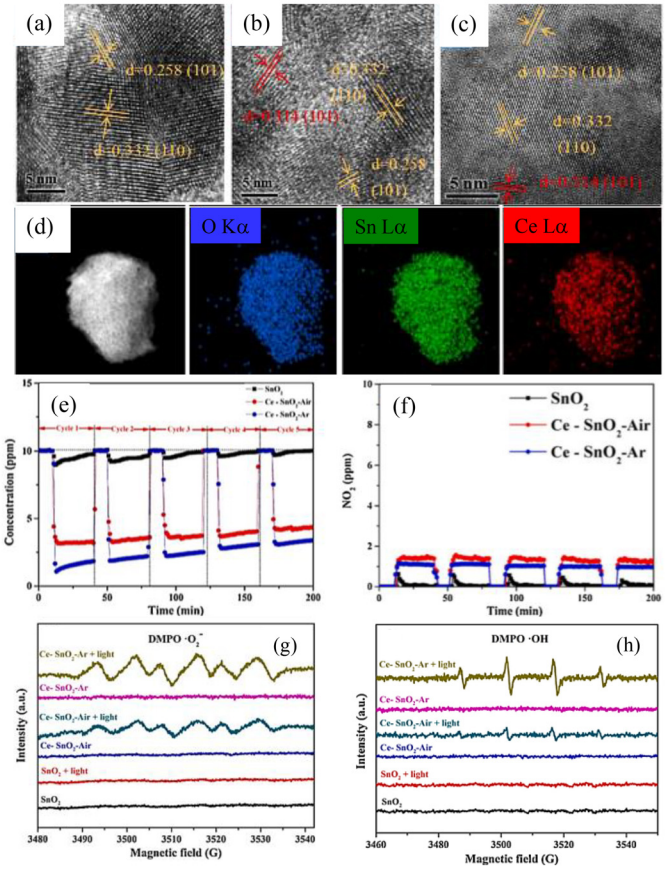

Fig. 4 High resolution-transmission electron microscopy (HR-TEM) images of SnO_2 (a) and Ce-doped SnO_2 annealed *ex situ* at 500 °C for 4 h under air (b) and Ar (c). The distances of 0.258 nm, 0.322 nm and 0.314 nm marked in the images correspond to the (101) and (110) crystal planes of SnO_2, and to the (101) plane of CeO_2, respectively. (d) Energy dispersive X-ray spectroscopy (EDXS) elemental maps for Ce-doped SnO_2 annealed under Ar. (e) NO removal curves under Vis-light illumination over these materials upon repeated cycling. (f) Corresponding real-time NO_2 yield. 5,5-Dimethyl-1-pyrroline-*N*-oxide (DMPO) spin-trapping EPR spectra of superoxide (g) and hydroxyl (h) radicals for SnO_2 and Ce-doped SnO_2 photocatalysts. Reprinted with permission from ref. 11. Copyright 2021, Elsevier.

upon cycling due to nitrite/nitrate accumulation on the system surface (Fig. 4e).

Among metal oxide systems, perovskite-type ones, with the general formula ABO_3, are 3D frameworks composed of corner-sharing BO_6 octahedra. Such a structure enables efficient charge transport, whereas the ability to accommodate OVs results in tailored electronic and optical properties. These characteristics are relevant for designing photocatalysts capable of harnessing Vis-light for NO_x abatement.[20] A relevant example is offered by $CaTiO_{3-\delta}$, a wide-bandgap perovskite ($E_G \approx 3.56$ eV), modified to introduce OVs through defect engineering.[56] These vacancies created intermediate energy levels within the bandgap, favorably promoting NO adsorption and subsequent photo-oxidation. Expanding on perovskite engineering, Lv *et al.*[33] developed an S-scheme heterojunction combining Bi-doped $La_2Ti_2O_7$ and La-doped $Bi_4Ti_3O_{12}$. The resulting interface yields a staggered alignment of conduction and valence bands, preserving the strong redox potentials of both the system components and promoting charge separation. This optimized heterostructure achieved 52% NO removal with minimal NO_2 generation (≈5.6 ppb), highlighting the synergistic effects of doping, defect engineering, and heterojunction construction. In a complementary approach, Zhang *et al.*[12] focused on the preparation of nano-heterostructured $LaFeO_3$–$SrTiO_3$ (LFO–STO) systems. $LaFeO_3$, a narrow bandgap perovskite, provides active NO adsorption sites, whereas $SrTiO_3$ improves charge transport due to the favorable CB alignment. Preliminary morphological analyses (Fig. 5a) revealed the obtainment of LFO spheres (diameters ≈ 0.1 ÷ 1 μm) coated with evenly dispersed, smaller STO NPs (Fig. 5b), with an intimate LFO/STO interfacial contact (Fig. 5c), advantageous for efficient charge transfer. Functional tests (Fig. 5d) showed that no NO conversion occurred under dark conditions ("blank" curve), whereas upon illumination the degradation was appreciably enhanced in comparison with individual LFO and STO thanks to the heterostructure formation. In fact, photoexcited electrons are transferred from LFO CB to the STO one, whereas holes flow in the opposite direction, thereby achieving enhanced charge separation (Fig. 5e). The oxidation process turned out to be driven by superoxide radicals as the

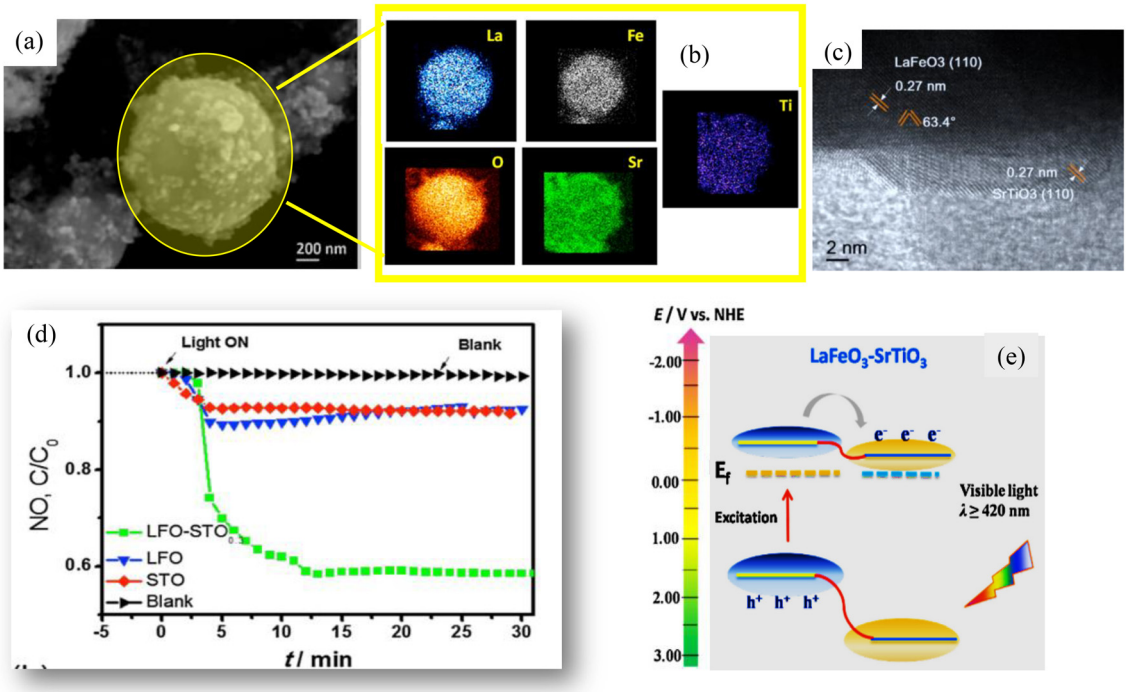

Fig. 5 (a) Representative scanning electron microscopy (SEM) image and (b) the corresponding EDXS chemical maps for a $LaFeO_3$–$SrTiO_3$ heterostructured system, obtained by ultrasonic spray pyrolysis, followed by solvothermal treatment. (c) HR-TEM image of the LFO/STO interface. (d) Photocatalytic NO removal profiles (C/C_0) as a function of time (Vis-light irradiation). (e) Schematic band energy diagram for LFO-STO heterostructures and the corresponding charge carrier separation under Vis illumination. Reprinted with permission from ref. 12. Copyright 2017, Elsevier.

main actors. In a complementary study, the photocatalytic performance of a Pb-free perovskite $(CH_3NH_3)_2AgInBr_6$ (MAIB), synthesized by a solvent-free mechanochemical route, was evaluated.[57] MAIB exhibited high NO removal efficiency under both UV-vis and Vis irradiation, but limited selectivity. Conversely, a composite integrating MgAlTi layered double hydroxide (MAIB/LDH) suppressed NO_2 emissions, reaching selectivity values up to 97%.

In summary, oxide-based heterostructures and perovskite materials represent appealing active platforms for photocatalytic NO_x degradation under Vis-light. The possibility of achieving fine tunability over material structure, defect engineering (such as oxygen vacancies), electronic band structures (ensuring improved charge carrier separation), morphology control, and doping levels results in enhanced and efficient NO_x degradation.

3.2 Plasmonic metal-containing photocatalysts

A viable and proficient route to boost $DeNO_x$ performances is offered by the introduction of plasmonic NPs in semiconducting materials. In fact, the resulting systems benefit from an increased Vis optical response thanks to localized surface plasmonic resonance (LSPR), leading to a coherent excitation of conduction electrons in metal particles,[20] as well as from the Schottky barriers at the metal/semiconductor interface, promoting the separation of photogenerated charge carriers and prolonging their lifetimes.[6] An interesting example in this regard is offered by the synthesis and characterization of Au/CeO_2 photocatalysts[43] (Fig. 6). Electron microscopy investigation (Fig. 6a–d) demonstrated the formation of CeO_2 nanorods (which were O-deficient), with interatomic distances of 0.27 and 0.19 nm, ascribed to the (200) and (220) crystallographic planes of cerium(IV) oxide, respectively. In the case of Au-containing systems (Fig. 6c and d), the interatomic distance of 0.24 nm is consistent with the (111) planes of metallic gold, whose NPs were successfully and homogeneously anchored on CeO_2 (Fig. 6e). Additional analyses showed that Au/CeO_2 exhibited remarkable NO removal at the LSPR wavelength position, in agreement with optical absorption spectra (Fig. 6f). The obtained results demonstrated the occurrence of an Au → CeO_2 charge transfer (Fig. 6g). Photocatalytic tests (Fig. 6h) pointed out that, for Au/CeO_2, NO removal appreciably increased in comparison with that by pristine CeO_2 (25%). In addition, the systems were characterized by excellent stability (Fig. 6i) and a high selectivity towards NO_3^- obtainment, with negligible NO_2 release (≈15 ppb). Real-time FT-IR spectroscopy demonstrated, for Au/CeO_2, enhanced NO oxidation *via* a dual-site activation pathway, where Au on CeO_2 promoted NO^+ formation, whereas OVs within CeO_2 (additionally induced by the LSPR effect) would facilitate $^{\bullet}O_2^-$ generation.

Sensitization with plasmonic NPs to improve Vis-light harvesting has also been performed for $SrTiO_3$, a perovskite-type semiconductor with a wide energy band gap (E_G = 3.2 eV).[6,20] In fact, Ag-modified-$SrTiO_3$ photocatalysts fabricated using a

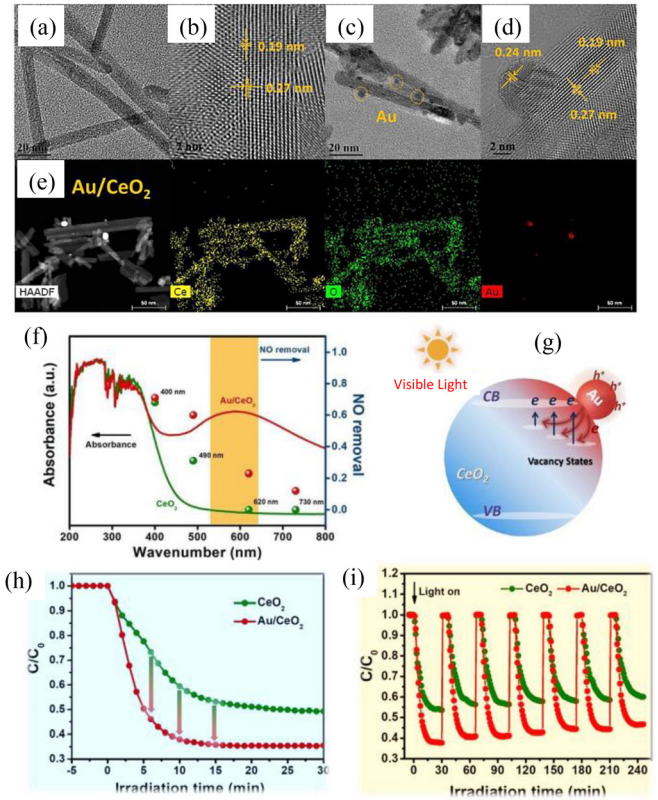

Fig. 6 TEM micrographs of CeO_2 (a and b) and Au/CeO_2 (c and d) photocatalysts. Bare CeO_2 nanorods were prepared using a hydrothermal process, whereas Au/CeO_2 catalysts were obtained using a deposition–precipitation method.[43] (e) EDXS mapping for Au/CeO_2. (f) Optical spectra and NO removal (left and right axes), and the corresponding electronic excitation (g). (h) Photocatalytic NO removal under Vis irradiation and (i) related cycling experiments. Reprinted with permission from ref. 43. Copyright 2020, Elsevier.

straightforward approach based on the use of silver-enriched wastewaters[6] delivered a NO_x photodegradation of ≈77% within 3 h under optimized processing conditions. In another study, Ma *et al.*[20] have reported on plasmonic silver metal modification of $SrTiO_3$ containing OVs, featuring an NO removal rate of 70% and good operational stability. A thorough characterization evidenced that the introduction of metallic Ag not only stimulated light absorption and charge transfer but also prevented the deactivation of oxygen vacancies. In fact, hot electrons generated by Ag *via* the LSPR effect can be efficiently transferred to $SrTiO_3$, thereby promoting a continuous OV generation. Furthermore, the formation of oxygen adsorption/activation sites at $Ag/SrTiO_3$ interfaces promotes significant $DeNO_x$ photocatalytic activity.

Advanced systems with improved functional characteristics can also be obtained by simultaneous doping and decoration with plasmonic NPs. A representative relevant work[42] concerns the fabrication of Au NP-loaded La-doped Bi_5O_7I microspheres *via* a solvothermal approach followed by *ex situ* thermal treatment and functionalization with Au NPs *via* a room-temperature chemical reduction.[48] The enhanced photocatalytic efficiency of the obtained nanocomposites resulted from the concurrence of La-ion doping, the presence of an oxygen vacancy, and the Au LSPR effect, producing strong Vis-light absorption. The reduced formation of intermediate NO_2, accompanied by the attractive stability, makes these systems interesting platforms for practical $DeNO_x$ end-uses.

A representative work on more complex heterostructures[26] was focused on the fabrication of $Ag/AgCl@BiOCl/Bi_{12}O_{17}Cl_2$ plasmonic composites by anchoring Ag/AgCl NPs on $BiOCl/Bi_{12}O_{17}Cl_2$ nanosheets *via* a deposition–precipitation method.[48] The synergetic LSPR effect of Ag NPs and the effective carrier separation brought about by the constructed junctions resulted in high stability and attractive Vis-light activated performances in the removal of NO at the indoor air level.

Plasmonic metal-based systems offer enhanced NO_x removal by extending light absorption into the visible range and enabling faster charge transfer dynamics. Their standout feature lies in their ability to activate under low-intensity light, making them attractive for indoor or shaded applications. However, their long-term environmental stability and cost-efficiency remain areas to be addressed for broader deployment.

3.3 Bismuth-containing photocatalysts

Bi-based photocatalysts have garnered increasing attention for $DeNO_x$ end-uses thanks to their amenable chemico-physical characteristics. Materials such as BiOX (X = Cl, Br, I), Bi_2WO_6, and $Bi_2O_2CO_3$ have a layered structure[58,59] facilitating e^-/h^+ separation, and their versatility opens the door to advanced strategies aimed at enhancing their performances and stability. At variance with different semiconductors, Bi-based materials exhibit narrow band gaps, enabling Vis-light absorption.[58] Rao *et al.*[60] demonstrated that $Bi_2O_2CO_3$ photoresponse could be significantly extended into the Vis region *via* engineering of OV sites within $[Bi_2O_2]^{2+}$ layers. These modifications yielded an NO removal efficiency of up to 50%, accompanied by a very modest NO_2 formation. In a complementary approach, Ran *et al.*[61] reported reversible UV-light induced defect engineering for $BiSbO_4$, exhibiting 42% NO removal efficiency with high selectivity and minimal nitrogen dioxide generation. Huo *et al.*[62–64] advanced the design of Bi-based photocatalysts using an ethylene glycol-assisted hydrothermal synthesis. In particular, the introduction of OVs in Bi_2WO_6 narrowed the bandgap and improved ROS generation for selective NO oxidation,[62] whereas carbonate intercalation in Bi_2MoO_6 created additional OVs and enhanced $^{\bullet}OH$ production, boosting NO elimination.[63] Combining both OVs and carbonate intercalation enabled obtaining the most efficient Bi_2WO_6 photocatalyst, achieving ≈55% NO removal and high durability.[64] Although OV introduction can remarkably enhance material performances, the effect is directly dependent on OV content and distribution. The latter interplay was demonstrated for $Bi_2Sn_2O_{7-x}$,[65] where only Sn-adjacent OVs improved the $DeNO_x$ capabilities by facilitating charge separation, whereas Bi-adjacent OVs acted as e^-/h^+ recombination

centres. Recent advances have emphasized the favourable combination of OVs and plasmonic Bi NP presence to extend light absorption and promote an improved electron/hole separation, as demonstrated for $Bi_{12}TiO_{20}$ nanofibers.[66] In particular, Bi^0 centers acted as electron sinks, whereas OVs facilitated ROS generation, ultimately resulting in selective NO → NO_3^- oxidation. Similarly, Xin *et al.*[18] synthesized Bi/BiOBr nanoflowers (average diameter ≈ 1.5 μm), whose morphology (Fig. 7a and b) consisted of abundant nanosheets. Photocatalytic activity tests toward ppb-NO elimination (Fig. 7c) demonstrated, in the best case, 63% NO removal with very low NO_2 formation (Fig. 7d). The nanoflower morphology and *in situ* Bi formation enhanced the surface area and electron capture, whereas the occurrence of OVs provided mid-gap electronic states responsible for Vis-light harvesting. Despite NO degradation being slightly lower at high relative humidity due to competitive H_2O and NO adsorption, nitrogen dioxide formation was appreciably reduced, thanks to the NO_2 interaction with H_2O and subsequent oxidation to NO_3^-. Such a strategy was also adopted in the case of $Bi@Bi_2GeO_5$[67] and $Bi/Bi_2O_{2-x}CO_3$ nanosheets,[68] achieving NO_x removal efficiencies up to ≈60% with low NO_2 generation. Another study was devoted to the liquid-phase preparation of mesoporous $Bi@Bi_2O_3$ nanospheres[69] that featured a well-defined morphology with a narrow pore size distribution (3.2–3.9 nm), appreciable Vis-light harvesting, and satisfactory NO adsorption ability. These characteristics, coupled with a strengthened LSPR Bi effect, were responsible for the excellent Vis-light NO_x photodegradation. Of particular interest is the complete NO_x conversion into nitrites/nitrates with no NO_2 production, a result opening the door to full-spectrum driven environmental purification.

The concurrent effect of plasmonic metal and OV presence was also investigated for $Bi@Bi_2Ti_2O_7$ systems prepared by a solvothermal method,[25] which exhibited a doubled efficiency in comparison with $Bi_2Ti_2O_7$ in the Vis-NIR activated removal of ppb-level NO. In fact, Bi^0 presence broadened the light response to the NIR region, inhibiting toxic intermediate formation and OV deactivation. In fact, the favourable synergy between OVs and Bi improved the photocatalytic efficiency, stability and selectivity of NO-to-NO_3^- conversion under Vis-NIR irradiation.

As regards doping strategies, Rao *et al.*[70] observed that Zn^{2+} doping in BiOI triggered OV generation, improving charge separation and ROS generation, leading to ≈54% NO removal with high selectivity. Guo *et al.*[71] demonstrated that post-synthesis Li intercalation into $Bi_4O_5Br_2$ introduced mid-gap states and enhanced carrier lifetimes to achieve up to ≈74% NO removal. The combination of rare-earth doping and plasmonic NPs, as in La^{3+}-doped Bi_5O_7I modified with Au,[42] provides a synergistic NO degradation enhancement by inducing OVs and narrowing the E_G, while Au NPs boost plasmonic activity and form Schottky barriers.

The construction of type-II and p–n heterojunctions has proved a very valuable toolkit to boost e^-/h^+ separation and

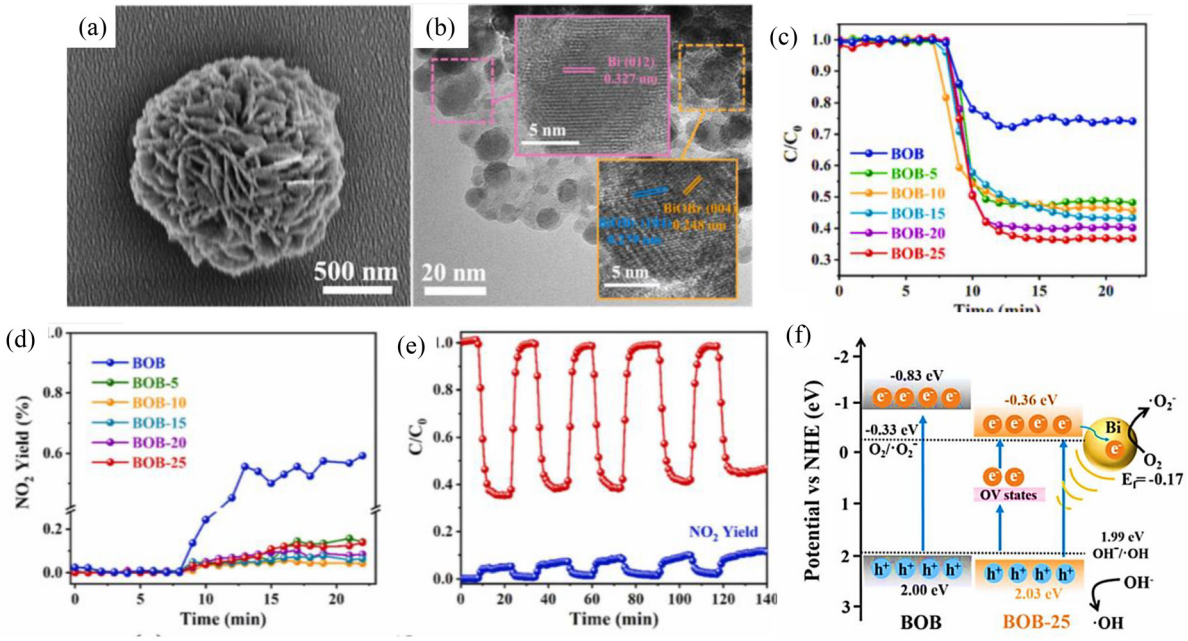

Fig. 7 Characterization of Bi/BiOBr photocatalysts prepared using a solvothermal approach in water–ethanol mixtures [denoted as BOB-*x* (*x* = 0, 5, 10, 15, 20, and 25 mL of ethanol in an overall solvent volume of 25 mL)].[18] SEM (a) and TEM (b) images of BOB-25. TEM analyses show two different types of lattice fringes with *d* spacings corresponding to the (104) and (004) planes of BiOBr (≈0.279 nm and 0.248 nm, respectively). The interplanar spacing of 0.327 nm corresponded to the (012) plane of Bi^0, confirming the surface presence of the latter. (c) Photocatalytic NO conversion and (d) the corresponding NO_2 formation over BOB-*x* specimens under Vis-light irradiation. (e) Cycling experiments over BOB-25. (f) Schematic energy band diagram, reporting approximate energy levels with respect to the normal hydrogen electrode (NHE) scale. Reprinted with permission from ref. 18. Copyright 2023, Elsevier.

trigger ROS generation under Vis illumination. For instance, $Bi_2Mo_3O_{12}$@$Bi_2O_2CO_3$ nanoflowers[72] showed improved NO removal thanks to their morphology, which increased surface reactivity and reduced charge carrier diffusion lengths. *In situ* IR analyses revealed efficient oxidation to NO_3^- *via* $^{\bullet}OH$ and $^{\bullet}O_2^-$, with minor NO_2 formation. In an analogous way, a $Bi_2O_2CO_3$/$ZnFe_2O_4$ p–n junction[73] achieved ≈30% NO removal with near-complete NO_2 suppression. A $Bi_4O_5I_2$/$FeVO_4$ type-II heterojunction reported by Chang *et al.*[74] combined hierarchical $Bi_4O_5I_2$ nanosheets with $FeVO_4$ spheres, reaching ≈40% NO_x removal with negligible NO_2 release. The robust and stable architecture improved Vis-light harvesting, charge separation, and $^{\bullet}O_2^-$ radical generation. In another study, Chang *et al.*[75] introduced a $Bi_4O_5Br_2$–graphene oxide (GO) composite *via* microwave-assisted synthesis, forming intimate interfaces and Schottky barriers that promoted charge extraction. Partial GO reduction enhanced both electron transfer and radiation harvesting, enabling obtaining ≈60% NO removal with a nitrate/nitrite selectivity of ≈92%.

Bismuth-based photocatalysts show excellent compatibility with Vis-light-driven NO_x abatement, particularly in humid and variable environments. Their intrinsic structural features allow selective and consistent NO conversion, with limited formation of harmful byproducts. This reliability makes them strong candidates for stable, real-world use under fluctuating atmospheric conditions.

3.4 Layered double hydroxides (LDHs)

LDHs are versatile functional materials characterized by highly tunable structures, derived from the brucite-like lattice of Mg$(OH)_2$, where divalent metal cations are substituted by trivalent ones, introducing a positive charge.[76] This excess charge is balanced by the incorporation of exchangeable anions and water. The general LDH formula is expressed as $[M_{1-x}^{II}M_x^{III}(OH)_2]^{x+}$ $X_{x/n}{}^{n-}\cdot mH_2O$, where M(II) and M(III) are divalent and trivalent cations, respectively, and X^{n-} represent the interlayer anions. In general, a large variety of metal ions and anions can be part of this flexible structure.[77] One of the main LDH advantages is their facile, scalable and environmentally benign synthesis.[78,79] Furthermore, LDHs exhibit a set of desirable properties for $DeNO_x$ applications, encompassing low toxicity, high stability, and excellent recyclability.[80,81] In particular, two features common to LDH-based $DeNO_x$ photocatalysts deserve due emphasis: (i) the key role of surface OH^- groups, converted into $^{\bullet}OH$ upon irradiation, thus promoting ROSs generation; and (ii) the high NO_2 adsorption capacity, enabling selectivities >90%.[82]

The first studies on the application of LDHs to photocatalytic $DeNO_x$ processes date back to 2018, when Rodriguez-Rivas *et al.*[83] investigated a series of Zn_xAl–CO_3 LDHs (x = 1.5–3.0) under UV irradiation. These materials demonstrated a $DeNO_x$ efficiency of 55% at the ppb level and retained the activity under prolonged operation. The systems displayed 90% selectivity toward NO_x degradation, significantly outperforming the benchmark TiO_2 P25. Accordingly, various strategies have been explored to impart Vis-light activity to LDH systems, among which is the controlled introduction of d and f-block elements (Cr, Fe, Cu or Eu). In the case of $Zn_3Al_{1-x}Cr_x$ (x = 0.2–1) LDHs, Cr introduction led to an enhanced surface area and enabled Vis-light absorption.[84] Notably, Cr presence inhibits e^-/h^+ recombination, thus enhancing $^{\bullet}OH$ and $^{\bullet}O_2^-$ formation and yielding enhanced performances. These Cr-containing LDHs could remove NO under Vis illumination, but with an efficiency lower than that obtained upon exposure to UV light (≈15% *vs.* 55%). Similar trends were observed for $Zn_3Al_{1-x}Fe_x$ (x = 0.2–0.5) and $Zn_{2-x}Cu_xCr$–CO_3 LDHs (x = 0.2–0.4).[34,85] Despite the fact that transition metal centers enabled Vis-light activity, NO removal efficiencies remained below 20%, suggesting that e^-/h^+ recombination dynamics are different in the case of UV and Vis-light activation. Thanks to their easy large-scale synthesis and low cost, LDHs have been proposed for real-world industrial applications. For instance, commercial mortars incorporating 1.0–2.0% Zn_2Cr LDH have been evaluated as a viable environmental solution for polluted urban air, maintaining the same Vis-light $DeNO_x$ performance as the corresponding powders.[86]

The nature of transition metal dopants has a significant effect. In fact, when small Al^{3+} amounts were replaced by Eu^{3+} in Mg_3Al and Zn_2Al LDHs, NO degradation efficiencies of up to 40% and 47% were achieved.[87,88] Besides extended light absorption, the presence of Eu^{3+} f levels in LDH plays a crucial role in suppressing e^-/h^+ recombination, enhancing ROS generation. A second strategy to boost photocatalytic activity involves the synthesis of LDHs at the nanoscale, taking advantage of the intrinsic properties of two-dimensional (2D) materials. In this regard, ultrathin Ni_xTi (x = 2, 3) LDH nanosheets with thicknesses of 2–5 nm can offer a high active site density, promoting an efficient and selective NO_x oxidation. Furthermore, their peculiar 2D morphology facilitates charge separation, resulting in NO removal efficiencies up to 20%.[44,89] An exceptional result was achieved with Ni_2Fe LDH thin nanosheets (3–4 nm), which removed up to 99% of NO. Compared to NiTi LDHs, the superior NiFe LDH performances were correlated to a high density of surface OVs, suppressing e^-/h^+ recombination and facilitating ROS formation.[90]

Based on the above studies, the next generation of LDH-based Vis-light $DeNO_x$ photocatalysts involves the construction of suitable heterojunctions to enhance charge carrier separation. A relevant example in this regard is offered by NiFe/MnO_2 systems, composed of NiFe–CO_3 LDHs and birnessite-type δ-MnO_2, that achieved a $DeNO_x$ efficiency of 40%, appreciably surpassing the ones of individual constituents.[19] The 2D morphology of MnO_2 and NiFe-LDH NPs was preserved in the obtained composites (Fig. 8a), and MnO_2 NPs were directly attached to NiFe-LDH nano-layers (Fig. 8b). The enhanced activity, with the best performances corresponding to a NiFe : MnO_2 10 : 1 ratio (Fig. 8c and d), was mainly related to the construction of heterojunctions that reduced e^-/h^+ recombination (Fig. 8e). Though charge carriers in MnO_2 rapidly recombine, electrons in NiFe-LDH CB can be transferred to the MnO_2 CB, while holes remain in the NiFe-LDH VB, thereby initiating photocatalytic reactions. In this case, $^{\bullet}O_2^-$ was

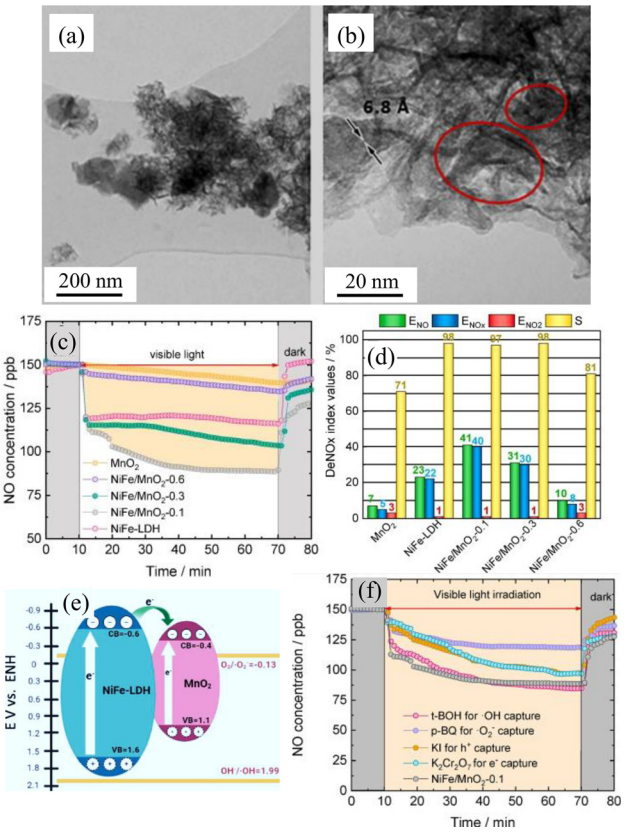

Fig. 8 Chemical–physical and functional characterization for NiFe-LDH/MnO_2 systems fabricated *via* co-precipitation and subsequent delamination.[19] The specimens were prepared starting from different amounts of MnO_2 powders (10, 30 and 60 mg) suspended in 5 mL of ethanol solution and named NiFe/MnO_2-0.1, NiFe/MnO_2-0.3 and NiFe/MnO_2-0.6, respectively. (a and b) TEM images of NiFe/MnO_2-0.1. The value of ≈7 Å is associated with the (00*l*) MnO_2 interlayer distances. (c) NO concentration profiles and (d) DeNO$_x$ indexes ((([NO$_x$] − [NO$_x$]$_{out}$/[NO$_x$]$_{in}$) × 100) during photocatalytic tests under Vis-light irradiation. Data for bare MnO_2 and NiFe-LDH are also reported. (e) Band diagram for the NiFe-LDH MnO_2 junction. (f) Trapping experiments for the NO photo-oxidation process over NiFe/MnO_2-0.1 (*t*-BOH = *tert*-butanol; *p*-BQ = *p*-benzoquinone). Reprinted with permission from ref. 19. Copyright 2024, Elsevier.

identified as the main reactive ROS, since ˙OH generation was limited by the VB position in the heterojunction (Fig. 8e).

Interestingly, the best result was obtained for NiTi-LDH/BiOBr composites, which exhibited complete removal of NO under Vis-light, an extraordinary performance maintained in successive running tests.[45] This successful result is ascribed to the adequate CB and VB edge positioning in the created type-II heterojunction, highly favoring the formation of ROS species.

LDH-based materials offer a promising balance between tunability, scalability, and environmental safety. While their overall NO$_x$ removal efficiencies under Vis-light are moderate compared to those of other systems, these can be easily boosted by appropriate doping of the structure or creation of adequate heterostructures. In addition, their structural adaptability and integration potential in construction materials open unique opportunities for large-area air purification technologies.

3.5 Carbon nitride-containing systems

In recent years, graphitic carbon nitride (gCN) has become a rising star as a metal-free photocatalyst due to its low cost, eco-friendly character, structural/compositional flexibility, and efficient Vis-light harvesting (E_G ≈ 2.7 eV) ability.[8,51,91–96] In fact, different works have focused on gCN in different forms for DeNO$_x$ applications. In 2014, Dong *et al.* reported on gCN deposition on ceramic foams using an *in situ* thermal approach,[91] recognizing the importance of photocatalyst immobilization for real-world end-uses. Materials annealed at 600 °C exhibited high and stable performances, with NO removal up to ≈77% under real indoor illumination. In order to overcome the main disadvantages of bare gCN, related to the limited surface area and the fast electron–hole recombination,[29,97] numerous research efforts have focused on thermal treatments, doping, chemical modification, modulation of N vacancies, and heterojunction construction.[9,51,92] Gu *et al.*[97] proposed an *ex situ* annealing method for the formation of nanosheets that yielded a DeNO$_x$ activity ≈3.0 times higher than that of bulk gCN. Such a result was attributed to enhanced ROS production, related to a lower e^-/h^+ recombination promoted by N defects. The latter could also be introduced by heating gCN under H_2,[95] yielding a higher NO removal thanks also to improved Vis-light harvesting.

The fabrication of heterocomposite gCN-containing DeNO$_x$ photocatalysts has been explored in different studies. Fang *et al.*[98] reported on a wet route to Au/gCN systems, achieving an exceptional NO removal of ≈93% upon illumination for 5 min. In fact, Au NPs facilitated charge separation and promoted O_2 transformation into $^{\bullet}O_2^-$ species. In another study, a porous gCN nanosheet photocatalyst modified with $CaCO_3$, a low-cost and abundant insulator, featured a NO photo-removal rate larger than 50%, surpassing that of pristine gCN (≈34%). This improvement was traced back to an extended Vis-light response and an enhanced charge carrier transfer, associated with the synergy between defects and $CaCO_3$, that can also efficiently chemisorb NO_2 and favorably contribute to the DeNO$_x$ process.[94] In a different study, Hu *et al.*[51] proposed an exfoliation approach and a hydrothermal route to a 3D aerogel comprising gCN quantum dots, graphene oxide, and $InVO_4$. These stable materials yielded an NO photo-removal efficiency up to 65%, related, in turn, to the layered aerogel structure, the construction of efficient heterojunctions, and the low charge carrier recombination. In other works, both lead-containing [$FAPbBr_3$, with FA = $CH(NH_2)_2$][9] and lead-free $Cs_3Bi_2Br_9$ perovskites[21] were synthesized *via in situ* growth on 3D gCN microspheres. The efficiency of Vis-light assisted NO removal, promoted by both $^{\bullet}O_2^-$ and ˙OH, was appreciably improved thanks to the formation of heterojunctions promoting e^-/h^+ separation.

High surface area photocatalysts for Vis-light-induced airborne NO$_x$ abatement were prepared by integrating Fe_3O_4 NPs and mesoporous gCN nanosheets.[8] Optimizing the treatment

temperature enabled obtaining an activity superior to that of commercial P25, with a parallel enhancement of the system selectivity and reusability. These results, related to the high surface area, suppressed electron–hole recombination, and improved Vis absorption, are of practical interest for the eventual production of active and environmentally friendly photocatalysts. In this regard, attractive perspectives are also offered by MgAlTi-LDH/gCN heterocomposites (Fig. 9).[40] For such systems, the main C and N photoelectron signals provided a fingerprint for the chemical environments expected in gCN (Fig. 9a–c). Upon going from bare gCN to composites with a higher carbon nitride content, the increasing $-NH_x$ contribution to the N 1s signal (Fig. 9c) favourably influenced the corresponding $DeNO_x$ activity, as a higher amino group concentration can promote improved gCN anchoring to MgAlTi-LDH and, consequently, enhanced gCN → MgAlTi-LDH charge transfer. Furthermore, defects resulting from amino-group presence can suppress e^-/h^+ recombination, thus enhancing the ultimate photoactivity of the material.[40] The Mg, Ti and Al peak features (Fig. 9d–f) were compatible with the presence of Mg(II), Ti(IV), and Al(III). Upon going from gCN to composites, the energies of C_1/C_2 bands and of N 1s ones (Fig. 9b and c) underwent an upward shift, while those of Mg 1s, Ti 2p and Al 2p signals presented a reduction with respect to bare MgAlTi (Fig. 9d–f), more marked upon increasing gCN content. These variations were traced back to the formation of heterojunctions featuring the gCN → MgAlTi electron transfer (Fig. 9g). Notably, unlike bare MgAlTi, the target heterocomposites exhibited Vis-light photoactivity, increasing with gCN amount (Fig. 9h). The best efficiency, obtained for the highest gCN content of 10%, surpassed the ones exhibited by various Vis-light $DeNO_x$ materials, opening the door to profitable real-world applications.[40]

Research dedicated to gCN composites has involved even ternary Z-scheme $Co(OH)_2/CeO_2$-gCN photocatalysts obtained *via* a hydrothermal method.[4] The presence of $Co(OH)_2$ as an

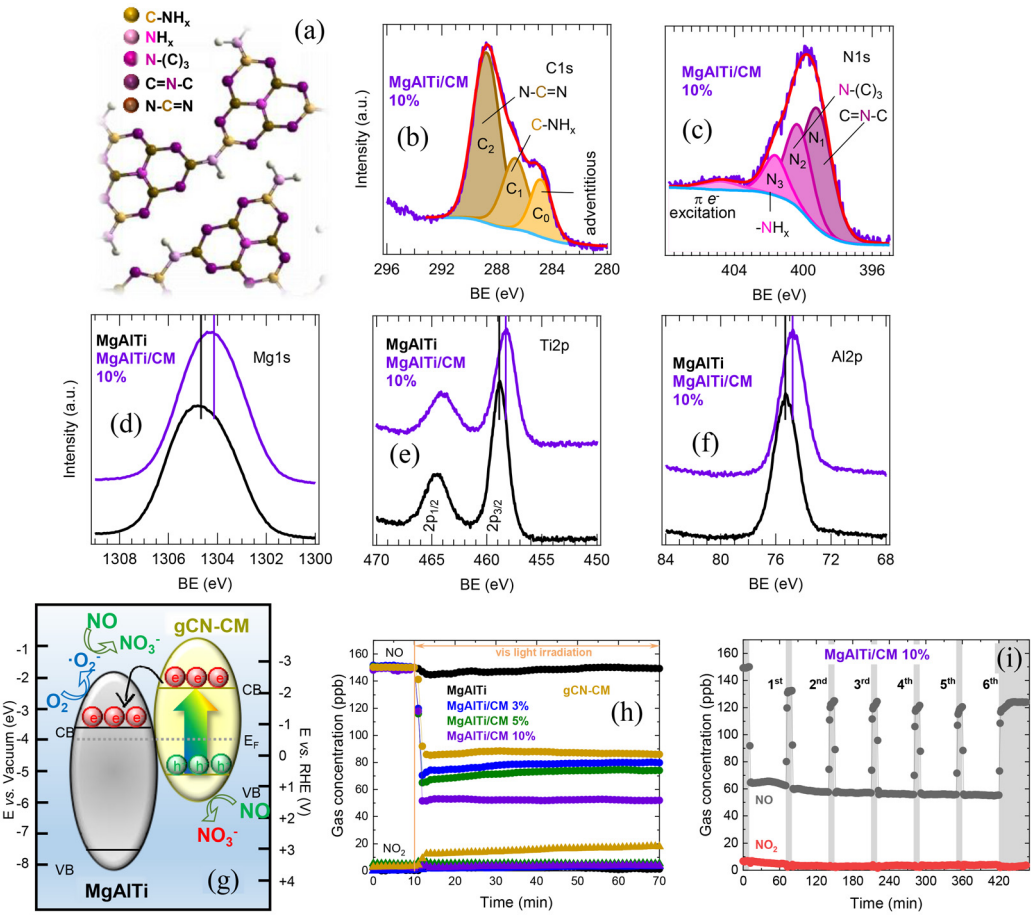

Fig. 9 Characterization of heterostructured MgAlTi-LDH/gCN composites obtained by mixing suspensions of both MgAlTi LDH (MgAlTi) and exfoliated graphitic carbon nitride (CM) in different amounts (3, 5, and 10% gCN mass weight).[40] (a) Sketch of the graphitic carbon nitride structure, with indications of non-equivalent carbon and nitrogen sites. X-ray photoelectron spectroscopy (XPS) signals for C 1s (b), N 1s (c), Mg 1s (d), Ti 2p (e), and Al 2p (f) pertaining to MgAlTi LDH/gCN (10%) and bare MgAlTi. In panel (b), component C_2 also resulted from the contribution of interlayer carbonate groups, whose occurrence is usually observed in LDHs. (g) Schematic representation of the gCN/MgAlTi heterojunction structure. (h) NO and NO_2 profiles recorded during $DeNO_x$ tests under Vis-light irradiation. Data for bare MgAlTi LDH are also plotted. (i) NO profiles for MgAlTi/CM 10% during consecutive cycles. Reprinted with permission from ref. 40. Copyright 2024, Wiley-VCH.

electron mediator between CeO_2 and gCN promoted electron transfer processes, providing also an extra reaction pathway for photocatalytic NO photodegradation. The synergistic partner contributions yielded not only an efficiency up to ≈54%, but also good recyclability and high selectivity towards nitrate formation. Among recent gCN modification strategies, intelligent active site engineering has involved single atom anchoring (M = Mg, Ti, Mn, Fe, Co).[17,29,93] An interesting example concerns the introduction of a single Zn atom in high amounts into the interlayer of pyrolytic gCN.[17] The enhanced Vis-light absorption and e^-/h^+ separation, as well as the promoted O_2 and NO activation, led to NO_3^- formation with low NO_2 release, an interesting starting point for possible pollution control *via* the use of single-atom catalysts.

In summary, the coupling of graphitic carbon nitride with other nanostructured materials has been employed to improve $DeNO_x$ photocatalytic performances, offering enhanced efficiency and selectivity, thanks to: (i) favorable chemical modifications; (ii) modulation of nitrogen vacancies; and (iii) heterojunction construction.

3.6 Carbon and graphene quantum dot-containing heterocomposites

The conjugated π structures of carbon quantum dots (CQDs) render them attractive electron transporters and acceptors, whereas the upconverted photoluminescence effect allows them to efficiently harvest solar light from the UV to the near-IR region.[28] In this scenario, attention has also been dedicated to graphene quantum dots (GQDs),[99] explored for the preparation of various composite materials since they possess non-zero band gaps and good dispersibility and can provide abundant reaction sites.[23]

As regards $DeNO_x$ applications, various composite systems integrating CQDs/GQDs and the materials targeted in the previous sections are available. In a work from Li *et al.*,[13] a novel composite photocatalyst combining CQDs, $SmFeO_3$, and attapulgite (ATP) clay mineral was synthesized using a sol–gel/impregnation process. $SmFeO_3$ NPs were evenly loaded on ATP and interacted directly with CQDs, whose content directly influenced NO conversion, yielding, in the best case, a rate of 90% and a selectivity of 100% under simulated sunlight. The authors proposed a Z-scheme mechanism, with CQDs acting as charge transfer mediators between $SmFeO_3$ and ATP. An interesting example of biocompatible CQD-containing photocatalysts, endowed with improved charge separation and high selectivity, is provided by CQD-modified FeOOH nanocomposites, prepared *via* an amenable hydrothermal process.[28] Investigation of material performances evidenced an improved NO removal efficiency, mainly mediated by superoxide species, in comparison with that of bare FeOOH, accompanied by moderate NO_2 release. The observed performance improvement was traced back to more effective light utilization and to suppressed e^-/h^+ recombination, thanks to enhanced FeOOH → CQDs electron transfer. The low toxicity of the developed materials, comprising highly abundant elements, ensures a negligible environmental footprint in view of eventual large-scale applications.

In a study by Liu *et al.*,[99] N-doped $Bi_2O_2CO_3$/[48]GQD composites, prepared by a facile process operating under ambient environment, showed a considerable $DeNO_x$ activity improvement with respect to the original N-doped $Bi_2O_2CO_3$ for Vis-light-activated photocatalytic removal of indoor air NO at ppb levels. This result was ascribed to the better light harvesting and enhanced charge separation of N-doped $Bi_2O_2CO_3$/GQDs during the photocatalytic process, in which the main active species were $^{\bullet}O_2^-$ radicals. *In situ* IR analyses indicated that NO could be efficiently adsorbed on the composite material surface and that, upon irradiation, the formation of both NO_2^- and NO_3^- species occurred. Although the majority of NO was probably completely converted into nitrate, nitrite accumulation did take place, in line with photocatalytic results that showed a gradual activity decrease under Vis irradiation. This issue has, of course, to be appropriately addressed for possible additional implementation.

Recently, Cui *et al.*[23] fabricated heterostructured GQDs/gCN Vis-light responsive photocatalysts by the hydrothermal combination of GQDs and gCN produced from pyrolysis of citric acid and melamine, respectively. The prepared materials were capable of degrading NO at ppm levels upon Vis-light illumination, and the best activity corresponded to an NO conversion rate of 90%, with a selectivity towards NO_3^- of 74%. These performances, accompanied by good cycling stability, were correlated with the inclusion of GQDs in gCN, promoting increased light harvesting, enhancing the surface area, and boosting e^-/h^+ separation thanks to the formation of type-II GQDs/gCN heterojunctions. More recently, Nie *et al.*[100] synthesized GQDs/BiOCl composites using a semi-solvothermal process. HR-TEM imaging (Fig. 10a–c) showed that GQDs were evenly dispersed on BiOCl nanoflakes, resulting in an increase of the specific surface area (from ≈5 to ≈35 $m^2\ g^{-1}$). The systems yielded an outstanding NO removal efficiency and a $DeNO_x$ index up to 81% and 0.55, respectively (Fig. 10d), under Vis-light illumination. Mechanistic studies confirmed enhanced electron–hole separation due to interfacial charge transfer, with $^{\bullet}O_2^-$ identified as the dominant ROS, whereas $^{\bullet}OH$ played a negligible role (Fig. 10e and f). This composite leveraged BiOCl/carbon nanostructure electronic interactions (Fig. 10g), offering a distinct pathway for selective and reusable NO_x photocatalysis.

Interestingly, GQDs have also been employed for preparing LDH-based heterojunctions with NO removal efficiencies reaching 55%. In GQDs/NiTi-LDH composites, GQDs improve Vis-light harvesting and form type-II heterojunctions, where electrons accumulate in the NiTi-LDH CB and holes remain in the GQD VB.[89] Remarkably, such materials maintained their activity even in the absence of light, making them the first reported $DeNO_x$ "day/night" photocatalysts.

In summary, CQDs and GQDs are excellent components for innovative composite systems for $DeNO_x$ applications. These materials generally show improved performances, demonstrating high NO conversion rates (up to 90%), good selectivity, and improved stability.

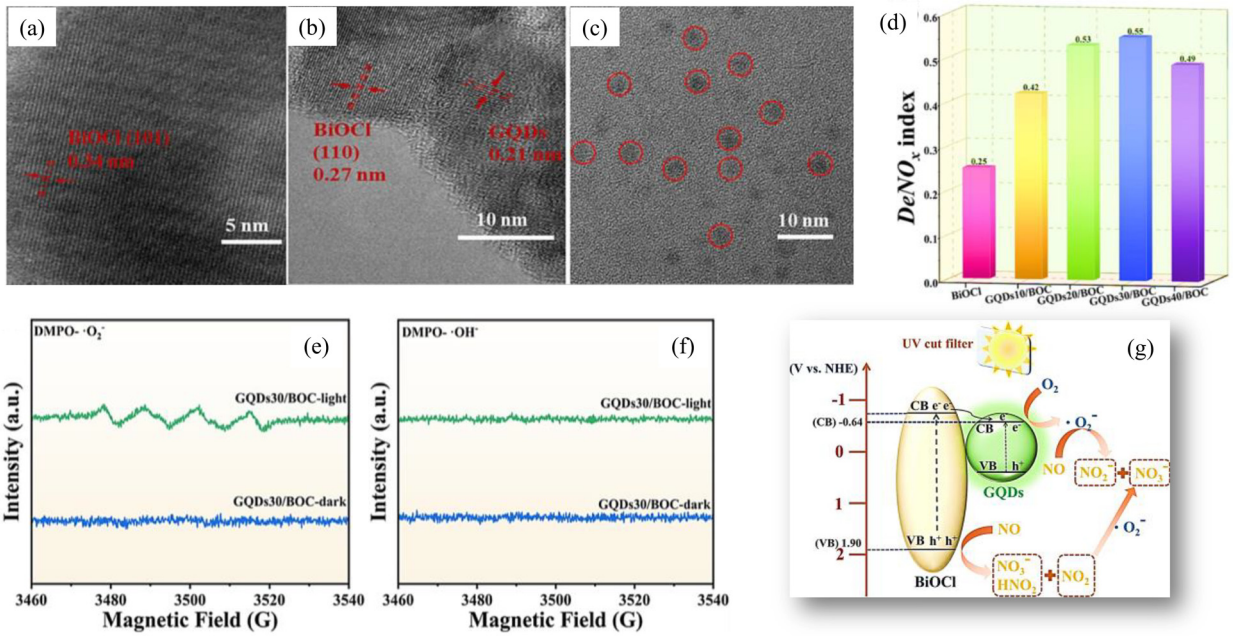

Fig. 10 Chemico-physical and functional characterization for GQDs/BiOCl.[100] The samples are denoted as GQDs*X*/BOC, where *X* corresponds to the GQD dosages of 10, 20, 30, or 40 mL added to 36 mL of ethylene glycol solution containing $Bi(NO_3)_3{\cdot}5H_2O$ (4.32 mmol) and NaCl (4.32 mmol). HR-TEM images of: (a) GQDs30/BOC; (b and c) GQDs. (d) $DeNO_x$ index.[100] DMPO spin-trapping EPR spectra of $^{\bullet}O_2^-$ (e) and $^{\bullet}OH$ (f) radicals for specimen GDQs30/BOC in the dark and under illumination. (g) Proposed mechanism of NO degradation promoted by GQDs/BOC photocatalysts. Reprinted with permission from ref. 100. Copyright 2024, Elsevier.

3.7 Other systems (MOFs, MXenes,...)

Further research works have been concerned with other kinds of Vis-light activated $DeNO_x$ photocatalysts, though the works available in this regard are less systematic. This section will provide a brief survey of selected representative results about these systems.

Oxynitrides, which are mixed anion materials, are promising Vis-light-driven photocatalysts due to their narrower band gap in comparison with those of various oxides. Wang *et al.*[101] reported on the synthesis of $(Zn_{1+x}Ge)(N_2O_x)$ NPs *via* nitridation of Zn_2GeO_4 prepared under solvothermal conditions. The obtained materials, endowed with high specific surface areas, exhibited Vis-light absorption, enabled by their relatively narrow band gap ($E_G \approx 2.7$ eV). These features, along with the presence of defects, are the cause of an enhancement of $DeNO_x$ photocatalytic activity, resulting in an NO_x conversion of ≈51%. In another work,[102] a low temperature solution route was used to prepare hollow $In(OH)_xS_y$ nanocubes featuring a porous structure and large surface areas, characterized by an attractive Vis-light photocatalytic activity promoted by both $^{\bullet}OH$ and $^{\bullet}O_2^-$ species.

Attention has also been devoted to MXenes, a new class of 2D transition metal carbides, nitrides, or carbonitrides featuring unique chemical and physical characteristics, encompassing high electrical conductivity, the presence of abundant functional groups, and the possibility of modulating Fermi level position by modifying the type of surface functional groups.[22] These properties can be harnessed to design Vis-light activated $DeNO_x$ photocatalysts with improved efficiency, charge carrier separation, and oxidative ability. Among the various relevant works available in the literature, which have been recently reviewed,[22,103] an interesting example is provided by Wang *et al.*,[104] who introduced Ti_3C_2 MXene QDs into SiC and obtained ≈75% efficiency in NO removal. This result was enabled by the construction of a 0D/2D heterojunction, which was effective for improved charge carrier separation, higher Vis-light absorption, and increased superoxide radical formation. These features, accompanied by the remarkable stability, provide a proficient pointer towards the design of improved active materials for $DeNO_x$ end-uses.

In the search for improved Vis-light-activated $DeNO_x$ photocatalysts, abundant natural minerals may offer a cost-effective and environmentally friendly alternative. In this context, Li *et al.*[105] reported that natural sand loaded with rhodamine B (RhB) exhibited a high activity in NO removal. A multi-technique characterization allowed the identification of $CaCO_3$ as a key component contributing to the enhancement in photoactivity. Photoactivity was also enhanced due to the introduction of RhB as a sensitizer, resulting in the generation of abundant electrons. In particular, the establishment of $CaCO_3 \rightarrow$ RhB charge transfer facilitated the adsorption and activation of both NO and O_2.

Other works also concerned the preparation of functionalized metal organic framework (MOF)-based systems, of significant interest for the target end-uses thanks to their large areas,

ordered porous structures, high stability, and remarkable structural variability.[106] In particular, MOF-containing single atom photocatalysts (see also 3.5) can maximize active metal sites, resulting in attractive functional performances.[107] In this context, an interesting study concerns the synthesis of a robust and efficient titanium MOF featuring an ultra-high loading of single atom Pt centers integrated into planar porphyrin units.[107] These systems enabled achieving an NO removal rate of up to 70%, accompanied by very good stability upon cycling. In the process, driven by both·$^{\bullet}$OH and $^{\bullet}O_2^-$, the presence of single atom Pt could promote the effective separation of electron–hole pairs and improve the ultimate photocatalytic activity. The use of atomically dispersed Pt has been exploited even by Hu *et al.*,[108] who reported on the fabrication of an MOF-derived ZnO/C system. Fig. 11a and b display the TEM images of Pt-ZnO/C and of Pt NPs-ZnO/C as a control specimen. In the latter case, some black spots with a size of ≈2 nm, corresponding to Pt nanoparticles, can be observed. Fig. 11c shows many aggregated bright spots (red circles) and a few isolated spots (blue squares), demonstrating the presence of Pt single atoms and nanoclusters. These bright spots are formed by 5–9 single Pt atoms. The recorded NO conversion rates (Fig. 11d) exceeded 80% for the Pt-ZnO/C system, a value appreciably higher than for the other cases, indicating that the incorporation of Pt single atoms/nanoclusters appreciably enhanced DeNO$_x$ activity. In parallel, an extremely low NO_2 release for the same system occurs (Fig. 11e), and the main oxidation products are indeed NO_3^-/NO_2^- ions, the latter being oxidized by O_2 to NO_3^- over time. The catalytic activity of Pt-ZnO/C catalysts could be quite well restored using UV radiation (Fig. 11f), although a non-negligible decrease upon cycling took place. EPR analyses (Fig. 11g and h) revealed·$^{\bullet}$OH and

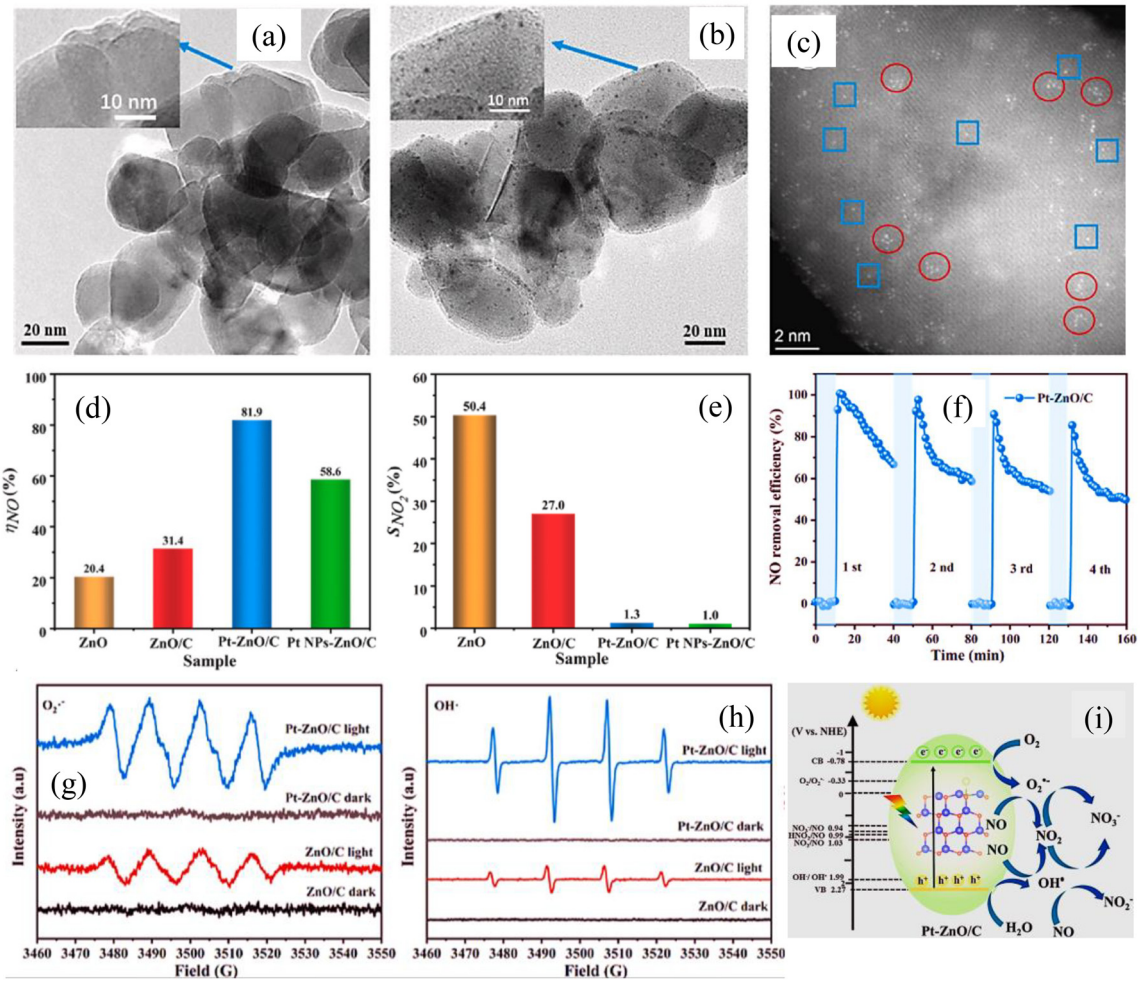

Fig. 11 Representative TEM images of (a) atomically dispersed Pt bridged with MOF-derived ZnO/C through carbon atoms (Pt-ZnO/C), (b) Pt NPs-ZnO/C, and (c) Pt-ZnO/C photocatalysts. The target systems were obtained *via* a liquid-phase route combining impregnation and calcination. (d) NO conversion rates[108] of ZnO, ZnO/C, Pt-ZnO/C, and Pt NPs-ZnO/C and photocatalysts. (e) Selectivity towards NO_2 [S_{NO_2} (%) = ($n_{NO_2,generated}$/$n_{NO,removed}$)100] for the same specimens under Vis-light irradiation for 30 min (NO inlet concentration = 11 ppm). (f) Cycling tests conducted on the Pt-ZnO/C catalyst. DMPO spin-trapping EPR spectra of superoxide (g) and hydroxyl (h) in the dark and under illumination for ZnO/C and Pt-ZnO/C catalysts. (i) Proposed mechanism of photocatalytic NO oxidation over Pt-ZnO/C catalysts under Vis-light irradiation. Reprinted with permission from ref. 108. Copyright 2023, Elsevier.

$^{\bullet}O_2^-$ radical signals upon Vis irradiation, indicating that both species contributed to NO photoremoval. Pt-ZnO/C catalysts yielded more intense signals for both ROSs in comparison with ZnO/C, underscoring the important role played by dispersed Pt in boosting functional performances.

Oxynitrides, MXenes, natural minerals, and MOFs show promising results for NO conversion due to their porous structures and large surface areas, enabling improved efficiency and charge carrier separation. These materials thus offer environmentally friendly photocatalysts for NO_x degradation under visible light.

3.8 Where, why, and how Vis-active photocatalysts work: toward real-world NO_x mitigation

The development of Vis-light-activated photocatalysts has opened new avenues for NO_x mitigation, particularly in urban environments and under solar irradiation. The present minireview has analyzed various alternative materials to TiO_2, each possessing specific features that determine their effectiveness under distinct conditions.

How do they work? Active photocatalysts for NO_x abatement rely fundamentally on the efficient generation and utilization of photogenerated charge carriers to drive redox reactions under Vis-light irradiation. This involves photon absorption to excite electrons across the bandgap, leading to the formation of $^{\bullet}OH$ and $^{\bullet}O_2^-$ ROSs, which oxidize NO to nitrites/nitrates. Materials with engineered band structures, through doping, OVs, plasmonic enhancement, or heterojunction construction, facilitate charge carrier separation and prolong their lifetimes. Notably, strategies like type-II heterojunction formation help to preserve strong redox potentials while reducing recombination, significantly improving selectivity towards nitrates over harmful NO_2.

Where do they perform best? These materials show optimal performance under conditions with sufficient Vis-light availability, such as urban environments with solar exposure (*e.g.*, building facades, road surfaces, *etc.*) or indoor environments with artificial lighting tailored to activate Vis-responsive catalysts. Systems like gCN, Bi-based materials, and LDH heterostructures exhibit robust performance under ambient conditions at ppb NO levels. In addition, materials that maintain activity in the presence of high humidity levels (*e.g.*, Bi/BiOBr, LDHs) are particularly well-suited for real-world, all-weather applications.

Why do they work? The superior performance of these materials arises from an arrangement of structural, electronic, and morphological features. Plasmonic nanoparticles (*e.g.*, Ag, Au, Bi) enhance Vis-light absorption *via* LSPR, simultaneously facilitating interfacial charge transfer processes. Oxygen vacancies serve as both active sites and electron traps, triggering NO adsorption and subsequent oxidation without undesirable NO_2 release. In addition, single-atom doping, quantum dot integration, and defect engineering enable precise control of the reaction pathway, fostering high selectivity and minimizing secondary pollution. Moreover, a large specific surface area and its functionalization facilitate the interaction and adsorption of reactant molecules, promoting their selective photo-oxidation. Ultimately, a successful Vis-active photocatalyst balances radiation absorption, charge separation, operational stability, and surface reactivity, tailored to the target environment and operational constraints.

4. Conclusions and outlook

In this minireview, we have summarized the most recent advances in the design and investigation of Vis-light activated photocatalysts, free from the widely investigated TiO_2, for the removal of gaseous NO_x and their conversion into non-toxic products. To our knowledge, although various general reviews on related topics are available, a contribution with a focus similar to the present one has no literature precedents so far. This field of investigation is of utmost interest to produce materials capable of efficiently exploiting the full spectrum of solar light, a largely available and virtually inexhaustible natural resource, for air purification purposes in various real-world environments. In fact, the utilization prospect encompasses both urban and industrial environments to ensure a higher breathable air quality and an improved safety level in a greener perspective.

The results summarized by the present overview highlight the extreme versatility and the huge potential of $DeNO_x$ photocatalytic processes, whose actual outcomes are directly dependent both on the semiconductor used and on the adopted processing routes. In particular, the large realm of functional nanomaterials offers an extremely attractive playground to tailor and boost the system's functional performances by modulating the system's nano-organization, morphology and chemical composition. These issues are clearly demonstrated by plasmonic photocatalysts, as well as by doped and heterostructured systems, whose mastering provides numerous degrees of freedom to enhance radiation harvesting and suppress electron–hole recombination, one of the main issues limiting the system photoactivity. Of course, tailoring the system's optical response is an essential aspect for further deployment of Vis-light activated $DeNO_x$ routes. The process's environmental footprint, in view of eventual scalability, is directly dependent even on the adopted photocatalysts, which should be free not only from heavy/toxic metals but also from critical raw materials. In this regard, attractive options are provided by nanostructures comprising gCN and C-based carbon dots and by LDH-based systems, providing a very flexible chemical playground. Further progress must also concern an optimization of service life, of key importance for practical end-uses.

Here we are up to and, on this basis, what's next? Undoubtedly, there is still a long way to go to ensure the necessary processes for real-world penetration of the present technology promoted using Vis-light. A key issue to be appropriately considered is related to the fact that the majority of photocatalysts discussed in this review are developed in powder form. This issue precludes important advances for future technological developments, considering that powdered

photocatalysts might be subjected to sintering/degradation phenomena, whereas supported systems can ensure higher stability and direct utilization/mounting in a variety of real-world environments. It is necessary for researchers to take a step forward and investigate these photocatalysts in real case studies, since their photocatalytic performance could vary substantially depending on the way the material is applied, the environmental conditions, the weather and the level of pollution in the urban center. Furthermore, regulatory agencies should get involved and communicate with nanomaterial researchers to formulate relevant guidelines regarding the manufacturing of the targeted photocatalysts and the operation of the corresponding $DeNO_x$ processes. These regulations can in fact provide important guidance upon establishing standardized production and quality control systems for nanomaterials to be developed on a medium and large scale. Last but not least, future activities should mitigate the detrimental effects of an incomplete conversion to nitrates, an open challenge still far from being completely met. The control of the selectivity system is, indeed, difficult to achieve *a priori*, and its optimization can be remarkably sustained by real-time process monitoring, as well as by theoretical calculations, which are of importance to gain pieces of information hardly accessible by experimental research. Towards this aim, adopting machine learning and artificial intelligence tools may help in the creation of novel, highly efficient nanomaterials with great specificity. The possibility of judiciously exploiting these convergent efforts represents, in perspective, a stepping stone in the transition from a *cook-and-look* approach to the manufacturing of $DeNO_x$ photocatalysts featuring tailored properties by design.

Author contributions

Conceptualization: D. B., C. M., B. G. and L. S.; literature review: D. B. and B. G; visualization, D. B., C. M. and L. S.; writing – original draft: D. B., B. G. and C. M.; writing – review and editing: C. M. and L. S.; supervision, C. M. and L. S. All authors have read and agreed to the published version of the manuscript.

Conflicts of interest

There are no conflicts to declare.

Data availability

No primary research results, software or code have been included, and no new data were generated or analysed as part of this review.

Supplementary information is available. See DOI: **https://doi.org/10.1039/d5nr03181h**.

Acknowledgements

The authors gratefully acknowledge financial support from Padova University (PDiSC#02BIRD2023-UNIPD RIGENERA, DOR 2023–2025), INSTM Consortium (TRI.25/013-CIMENTO), and Agencia Estatal de Investigación (Spain; projects MCIN PID2020-117516GB-I00/AEI/10.13039/501100011033 and MCIN PID2024-156242OB-I00 /AEI/10.13039/501100011033).

References

1 R. Fuller, P. J. Landrigan, K. Balakrishnan, G. Bathan, S. Bose-O'Reilly, M. Brauer, J. Caravanos, T. Chiles, A. Cohen, L. Corra, M. Cropper, G. Ferraro, J. Hanna, D. Hanrahan, H. Hu, D. Hunter, G. Janata, R. Kupka, B. Lanphear, M. Lichtveld, K. Martin, A. Mustapha, E. Sanchez-Triana, K. Sandilya, L. Schaefli, J. Shaw, J. Seddon, W. Suk, M. M. Téllez-Rojo and C. Yan, *Lancet Planet. Health*, 2022, **6**, e535–e547.
2 C. Duclairoir Poc, S. Depayras, N. Orange, M. Feuilloley, H. J. Heipieper and T. Kondakova, in *Emerging Pollutants - Some Strategies for the Quality Preservation of Our Environment*, ed. S. Soloneski and M. L. Larramendy, IntechOpen, Rijeka, 2018.
3 A. Talaiekhozani, S. Rezania, K.-H. Kim, R. Sanaye and A. M. Amani, *J. Cleaner Prod.*, 2021, **278**, 123895.
4 Z. Xiao, H. Do, A. Yusuf, H. Jia, H. Ma, S. Jiang, J. Li, Y. Sun, C. Wang, Y. Ren, G. Z. Chen and J. He, *J. Hazard. Mater.*, 2024, **462**, 132744.
5 T. Xue, J. Li, L. Chen, K. Li, Y. Hua, Y. Yang and F. Dong, *Chem. Sci.*, 2024, **15**, 9026–9046.
6 M. F. Ordoñez, G. Cerrato, A. Giordana, A. Di Michele, E. Falletta and C. L. Bianchi, *J. Environ. Chem. Eng.*, 2023, **11**, 110368.
7 M. Sompornrattanaphan, T. Thongngarm, P. Ratanawatkul, C. Wongsa and J. J. Swigris, *Asian Pac. J. Allergy Immunol.*, 2020, **38**, 19–28.
8 M. Irfan, M. Sevim, Y. Koçak, M. Balci, Ö. Metin and E. Ozensoy, *Appl. Catal., B*, 2019, **249**, 126–137.
9 B. Xie, D. Chen, N. Li, Q. Xu, H. Li, J. He and J. Lu, *Chem. Eng. J.*, 2022, **430**, 132968.
10 T. H. Panigrahi, S. R. Sahoo, G. Murmu, D. Maity and S. Saha, *Prog. Solid State Chem.*, 2022, **68**, 100380.
11 X. Song, G. Qin, G. Cheng, W. Jiang, X. Chen, W. Dai and X. Fu, *Appl. Catal., B*, 2021, **284**, 119761.
12 Q. Zhang, Y. Huang, S. Peng, Y. Zhang, Z. Shen, J.-j. Cao, W. Ho, S. C. Lee and D. Y. H. Pui, *Appl. Catal., B*, 2017, **204**, 346–357.
13 X. Li, H. Shi, T. Wang, Y. Zhang, S. Zuo, S. Luo and C. Yao, *Appl. Surf. Sci.*, 2018, **456**, 835–844.
14 Y. Lu, M. Chen, L. Jiang, J.-j. Cao, H. Li, S. C. Lee and Y. Huang, *Environ. Chem. Lett.*, 2022, **20**, 3905–3925.
15 J. Balbuena, M. Cruz-Yusta and L. Sánchez, *J. Nanosci. Nanotechnol.*, 2015, **15**, 6373–6385.

16 D. Barreca and C. Maccato, *CrystEngComm*, 2023, **25**, 3968–3987.
17 R. Zhang, Y. Cao, D. E. Doronkin, M. Ma, F. Dong and Y. Zhou, *Chem. Eng. J.*, 2023, **454**, 140084.
18 Y. Xin, Q. Zhu, T. Gao, X. Li, W. Zhang, H. Wang, D. Ji, Y. Huang, M. Padervand, F. Yu and C. Wang, *Appl. Catal., B*, 2023, **324**, 122238.
19 M. Á. Oliva, D. Giraldo, P. Almodóvar, F. Martín, M. L. López, I. Pavlovic and L. Sánchez, *Chem. Eng. J.*, 2024, **489**, 151241.
20 H. Ma, W. Yang, H. Tang, Y. Pan, W. Li, R. Fang, Y. Shen and F. Dong, *J. Hazard. Mater.*, 2023, **452**, 131269.
21 B. Xie, D. Chen, N. Li, Q. Xu, H. Li and J. Lu, *Chem. Eng. J.*, 2023, **452**, 139662.
22 J. O. Ighalo, M. L. Smith, A. A. Mayyahi and P. B. Amama, *Appl. Catal., B*, 2024, **358**, 124352.
23 Y. Cui, X. Huang, T. Wang, L. Jia, Q. Nie, Z. Tan and H. Yu, *Carbon*, 2022, **191**, 502–514.
24 G. A. K. M. Rafiqul Bari, M. Islam and J.-H. Jeong, *Metals*, 2024, **14**, 423.
25 Q. Zhu, R. Hailili, Y. Xin, Y. Zhou, Y. Huang, X. Pang, K. Zhang, P. K. J. Robertson, D. W. Bahnemann and C. Wang, *Appl. Catal., B*, 2022, **319**, 121888.
26 W. Zhang, X. a. Dong, Y. Liang, Y. Sun and F. Dong, *Appl. Surf. Sci.*, 2018, **455**, 236–243.
27 M. Cruz-Yusta, M. Sánchez and L. Sánchez, Metal oxide nanomaterials for nitrogen oxides removal in urban environments, in *Tailored Functional Oxide Nanomaterials: From Design to Multi-Purpose Applications*, ed. D. Barreca and C. Maccato, Wiley-VCH, 2022, pp. 229–276.
28 Y. Huang, Y. Gao, Q. Zhang, Y. Zhang, J.-j. Cao, W. Ho and S. C. Lee, *J. Hazard. Mater.*, 2018, **354**, 54–62.
29 Z. Hu, Y. Zhang, Y. Wang, J. Huang, S. Yang and H. Li, *Appl. Catal., B*, 2024, **350**, 123948.
30 S. E. Manahan, *Environmental Chemistry*, CRC Press, Taylor & Francis Group, 9th edn, 2010.
31 **https://environment.ec.europa.eu/topics/air/air-quality/eu-air-quality-standards_en**.
32 **https://iris.who.int/handle/10665/345329**.
33 L. Lv, L. Lei, Q.-W. Chen, C.-L. Yin, H. Fan and J.-P. Zhou, *Appl. Catal., B*, 2024, **343**, 123464.
34 J. Fragoso, M. A. Oliva, L. Camacho, M. Cruz-Yusta, G. de Miguel, F. Martin, A. Pastor, I. Pavlovic and L. Sánchez, *Chemosphere*, 2021, **275**, 130030.
35 R. Sugrañez, J. Balbuena, M. Cruz-Yusta, F. Martín, J. Morales and L. Sánchez, *Appl. Catal., B*, 2015, **165**, 529–536.
36 J. Balbuena, J. M. Calatayud, M. Cruz-Yusta, P. Pardo, F. Martín, J. Alarcón and L. Sánchez, *Dalton Trans.*, 2018, **47**, 6590–6597.
37 J. Balbuena, M. Cruz-Yusta, A. Pastor and L. Sánchez, *J. Alloys Compd.*, 2018, **735**, 1553–1561.
38 G. Carraro, R. Sugrañez, C. Maccato, A. Gasparotto, D. Barreca, C. Sada, M. Cruz-Yusta and L. Sánchez, *Thin Solid Films*, 2014, **564**, 121–127.
39 A. Folli, J. Z. Bloh, M. Strøm, T. Pilegaard Madsen, T. Henriksen and D. E. Macphee, *J. Phys. Chem. Lett.*, 2014, **5**, 830–832.
40 L. Marín, M. Benedet, C. Maccato, G. A. Rizzi, O. I. Lebedev, I. Pavlovic, L. Sánchez and D. Barreca, *Adv. Sustainable Syst.*, 2024, **8**, 2400496.
41 A. Pastor, J. Balbuena, M. Cruz-Yusta, I. Pavlovic and L. Sánchez, *Chem. Eng. J.*, 2019, **368**, 659–667.
42 J. Zhang, G. Zhu, S. Li, F. Rao, Q.-U. Hassan, J. Gao, Y. Huang and M. Hojamberdiev, *ACS Appl. Mater. Interfaces*, 2019, **11**, 37822–37832.
43 H. Shang, S. Huang, H. Li, M. Li, S. Zhao, J. Wang, Z. Ai and L. Zhang, *Chem. Eng. J.*, 2020, **386**, 124047.
44 A. Pastor, C. Chen, G. de Miguel, F. Martin, M. Cruz-Yusta, J.-C. Buffet, D. O'Hare, I. Pavlovic and L. Sánchez, *Chem. Eng. J.*, 2022, **429**, 132361.
45 M. A. Oliva, J. Ortiz-Bustos, M. Cruz-Yusta, F. Martin, I. del Hierro, Y. Pérez, I. Pavlovic and L. Sánchez, *Chem. Eng. J.*, 2023, **470**, 144088.
46 B. Rhimi, M. Padervand, H. Jouini, S. Ghasemi, D. W. Bahnemann and C. Wang, *J. Environ. Chem. Eng.*, 2022, **10**, 108566.
47 Z. Fang, M. Zhou, Z. Lin, C. Yang, Y. Hou, J. C. Yu, J. Zhang and X. Wang, *Appl. Catal., B*, 2024, **353**, 124022.
48 The target system could have been reported even among Bi-containing photocatalysts in section 3.3, but it is discussed here as an example of plasmonic photocatalysts.
49 A. Gasparotto, G. Carraro, C. Maccato, C. Sada, J. Balbuena, M. Cruz-Yusta, L. Sánchez, N. Vodišek, U. Lavrencic Štangar and D. Barreca, *CrystEngComm*, 2018, **20**, 1282–1290.
50 D. Barreca, F. Gri, A. Gasparotto, T. Altantzis, V. Gombac, P. Fornasiero and C. Maccato, *Inorg. Chem.*, 2018, **57**, 14564–14573.
51 J. Hu, D. Chen, N. Li, Q. Xu, H. Li, J. He and J. Lu, *Appl. Catal., B*, 2018, **236**, 45–52.
52 J. Fragoso, D. Barreca, L. Bigiani, C. Sada, O. I. Lebedev, E. Modin, I. Pavlovic, L. Sánchez and C. Maccato, *ACS Appl. Mater. Interfaces*, 2021, **13**, 44520–44530.
53 J. Fragoso, D. Barreca, L. Bigiani, A. Gasparotto, C. Sada, O. I. Lebedev, E. Modin, I. Pavlovic, L. Sánchez and C. Maccato, *Chem. Eng. J.*, 2022, **430**, 132757.
54 D. P. H. Tran, M.-T. Pham, Y.-F. Wang and S.-J. You, *J. Ind. Eng. Chem.*, 2023, **127**, 343–355.
55 S. N. Nguyen, T. K. Truong, S.-J. You, Y.-F. Wang, T. M. Cao and V. V. Pham, *ACS Omega*, 2019, **4**, 12853–12859.
56 J. Chen, C. Wang, J. Li, J. Ni, Y. Tang, J. T. S. Irvine and C. Ni, *Chem. Eng. J.*, 2023, **455**, 140896.
57 J. Estrada-Pomares, M. d. l. Á. Oliva, L. Sánchez and G. de Miguel, *J. Environ. Chem. Eng.*, 2025, **13**, 114934.
58 X. Lu, L. Wang, Z. Li, Z. Wang, Y. Gan and R. Hailili, *ACS Sustainable Chem. Eng.*, 2024, **12**, 11444–11466.
59 X. Li, Q. Dong, F. Li, Q. Zhu, Q. Tian, L. Tian, Y. Zhu, B. Pan, M. Padervand and C. Wang, *Appl. Catal., B*, 2024, **340**, 123238.

60 F. Rao, G. Zhu, W. Zhang, Y. Xu, B. Cao, X. Shi, J. Gao, Y. Huang, Y. Huang and M. Hojamberdiev, *ACS Catal.*, 2021, **11**, 7735–7749.
61 M. Ran, H. Wang, W. Cui, J. Li, P. Chen, Y. Sun, J. Sheng, Y. Zhou, Y. Zhang and F. Dong, *ACS Appl. Mater. Interfaces*, 2019, **11**, 47984–47991.
62 W. C. Huo, X. a. Dong, J. Y. Li, M. Liu, X. Y. Liu, Y. X. Zhang and F. Dong, *Chem. Eng. J.*, 2019, **361**, 129–138.
63 W. Huo, W. Xu, T. Cao, Z. Guo, X. Liu, G. Ge, N. Li, T. Lan, H.-C. Yao, Y. Zhang and F. Dong, *J. Colloid Interface Sci.*, 2019, **557**, 816–824.
64 W. Huo, W. Xu, T. Cao, X. Liu, Y. Zhang and F. Dong, *Appl. Catal., B*, 2019, **254**, 206–213.
65 Y. Lu, M. Chen, T. Huang, Y. Huang, J.-j. Cao, H. Li, W. Ho and S. C. Lee, *Environ. Sci.: Nano*, 2021, **8**, 1927–1933.
66 H. Liu, H. Mei, N. Miao, L. Pan, Z. Jin, G. Zhu, J. Gao, J. Wang and L. Cheng, *Chem. Eng. J.*, 2021, **414**, 128748.
67 X. Li, W. Zhang, W. Cui, J. Li, Y. Sun, G. Jiang, H. Huang, Y. Zhang and F. Dong, *Chem. Eng. J.*, 2019, **370**, 1366–1375.
68 Y. Lu, Y. Huang, Y. Zhang, T. Huang, H. Li, J.-j. Cao and W. Ho, *Chem. Eng. J.*, 2019, **363**, 374–382.
69 P. Zhang, Y. Huang, Y. Rao, M. Chen, X. Li, W. Ho, S. Lee and J. Cao, *Chem. Eng. J.*, 2021, **406**, 126910.
70 F. Rao, G. Zhu, M. Hojamberdiev, W. Zhang, S. Li, J. Gao, F. Zhang, Y. Huang and Y. Huang, *J. Phys. Chem. C*, 2019, **123**, 16268–16280.
71 Y.-Y. Guo, W.-B. Zhang, Y.-N. Yang and C. Wang, *J. Phys. Chem. Solids*, 2021, **159**, 110256.
72 W. Huo, T. Cao, W. Xu, Z. Guo, X. Liu, H.-C. Yao, Y. Zhang and F. Dong, *Chin. J. Catal.*, 2020, **41**, 268–275.
73 Y. Huang, D. Zhu, Q. Zhang, Y. Zhang, J.-j. Cao, Z. Shen, W. Ho and S. C. Lee, *Appl. Catal., B*, 2018, **234**, 70–78.
74 F. Chang, Z. Wei, J. Wang, S. Zhao and D.-g. Liu, *Mater. Chem. Phys.*, 2022, **291**, 126729.
75 F. Chang, C. Yang, J. Wang, B. Lei, S. Li and H. Kim, *Sep. Purif. Technol.*, 2021, **266**, 118237.
76 F. Cavani, F. Trifirò and A. Vaccari, *Catal. Today*, 1991, **11**, 173–301.
77 D. G. Evans and R. C. T. Slade, in *Layered Double Hydroxides*, ed. X. Duan and D. G. Evans, Springer Berlin Heidelberg, Berlin, Heidelberg, 2006, pp. 1–87.
78 Z.-H. Xie, H.-Y. Zhou, C.-S. He, Z.-C. Pan, G. Yao and B. Lai, *Chem. Eng. J.*, 2021, **414**, 128713.
79 S. Tang, Y. Yao, T. Chen, D. Kong, W. Shen and H. K. Lee, *Anal. Chim. Acta*, 2020, **1103**, 32–48.
80 L. Mohapatra and K. Parida, *J. Mater. Chem. A*, 2016, **4**, 10744–10766.
81 S.-F. Ng, M. Y. L. Lau and W.-J. Ong, *Sol. RRL*, 2021, **5**, 2000535.
82 X. Lv, J. Zhang, X. Dong, J. Pan, W. Zhang, W. Wang, G. Jiang and F. Dong, *Appl. Catal., B*, 2020, **277**, 119200.
83 F. Rodriguez-Rivas, A. Pastor, C. Barriga, M. Cruz-Yusta, L. Sánchez and I. Pavlovic, *Chem. Eng. J.*, 2018, **346**, 151–158.
84 F. Rodriguez-Rivas, A. Pastor, G. de Miguel, M. Cruz-Yusta, I. Pavlovic and L. Sánchez, *Sci. Total Environ.*, 2020, **706**, 136009.
85 A. Pastor, F. Rodriguez-Rivas, G. d. Miguel, M. Cruz-Yusta, F. Martin, I. Pavlovic and L. Sánchez, *Chem. Eng. J.*, 2020, **387**, 124110.
86 J. Fragoso, J. Balbuena, M. Cruz-Yusta, I. Pavlovic, M. Sánchez and L. Sánchez, *Constr. Build. Mater.*, 2023, **394**, 132241.
87 A. Pastor, C. Chen, G. de Miguel, F. Martín, M. Cruz-Yusta, D. O'Hare, I. Pavlovic and L. Sánchez, *Chem. Eng. J.*, 2023, **471**, 144464.
88 M. d. l. Á. Oliva, C. Chen, G. de Miguel, D. O'Hare, I. Pavlovic, L. Sánchez and A. Pastor, *Chemosphere*, 2024, **361**, 142555.
89 J. Fragoso, A. Pastor, M. Cruz-Yusta, F. Martin, G. de Miguel, I. Pavlovic, M. Sánchez and L. Sánchez, *Appl. Catal., B*, 2023, **322**, 122115.
90 H. Li, H. Zhu, Y. Shi, H. Shang, L. Zhang and J. Wang, *Environ. Sci. Technol.*, 2022, **56**, 1771–1779.
91 F. Dong, Z. Wang, Y. Li, W.-K. Ho and S. C. Lee, *Environ. Sci. Technol.*, 2014, **48**, 10345–10353.
92 Z. Song, L. Xu, C. Xie, Y. Liu, Z. Han and J. Lu, *Chem. Eng. J.*, 2025, **508**, 161143.
93 K. Li, N. Kang, X. Li, Z. Wang, N. Wang, Y. Kuwahara, K. Lv and H. Yamashita, *Appl. Catal., B*, 2024, **355**, 124163.
94 K. Li, W. Zhou, X. Li, Q. Li, S. A. C. Carabineiro, S. Zhang, J. Fan and K. Lv, *J. Hazard. Mater.*, 2023, **442**, 130040.
95 J. Liao, W. Cui, J. Li, J. Sheng, H. Wang, X. Dong, P. Chen, G. Jiang, Z. Wang and F. Dong, *Chem. Eng. J.*, 2020, **379**, 122282.
96 Z. Wang, X. Shi, M. Chen, J. Cao, W. Ho, S. Lee, C. Wang and Y. Huang, *Environ. Chem. Lett.*, 2023, **21**, 2913–2952.
97 Z. Gu, Y. Asakura and S. Yin, *Nanotechnology*, 2020, **31**, 114001.
98 Z. Fang, M. Zhou, J. Tao, Y. Hou, W.-K. Ho, C. Yang, J. C. Yu, M. Anpo, J. Zhang and X. Wang, *Appl. Catal., B*, 2025, **369**, 125164.
99 Y. Liu, S. Yu, Z. Zhao, F. Dong, X. A. Dong and Y. Zhou, *J. Phys. Chem. C*, 2017, **121**, 12168–12177.
100 Q. Nie, L. Jia, J. Luan, Y. Cui, J. Liu, Z. Tan and H. Yu, *Chem. Eng. Sci.*, 2024, **285**, 119614.
101 J. Wang, Y. Asakura and S. Yin, *Nanoscale*, 2019, **11**, 20151–20160.
102 S. Ge and L. Zhang, *Environ. Sci. Technol.*, 2011, **45**, 3027–3033.
103 A. A. Mayyahi, S. Sarker, B. M. Everhart, X. He and P. B. Amama, *Mater. Today Commun.*, 2022, **32**, 103835.
104 H. Wang, R. Zhao, H. Hu, X. Fan, D. Zhang and D. Wang, *ACS Appl. Mater. Interfaces*, 2020, **12**, 40176–40185.
105 Y.-H. Li, B.-F. Chen, S. A. C. Carabineiro, Y.-Y. Duan, P. Tan, W.-K. Ho and F. Dong, *Rare Met.*, 2024, **43**, 543–554.
106 Y. C. López, H. Viltres, N. K. Gupta, P. Acevedo-Peña, C. Leyva, Y. Ghaffari, A. Gupta, S. Kim, J. Bae and K. S. Kim, *Environ. Chem. Lett.*, 2021, **19**, 1295–1334.
107 H. Feng, H. Li, X. Liu, Y. Huang, Q. Pan, R. Peng, R. Du, X. Zheng, Z. Yin, S. Li and Y. He, *Chem. Eng. J.*, 2022, **428**, 132045.
108 L. Hu, J. Liu, X. Huang, Q. Nie, P. Liu, Z. Tan and H. Yu, *Carbon*, 2023, **214**, 118299.